

Extreme value laws in dynamical systems under physical observables

Mark P. Holland,¹ Renato Vitolo,^{1,*} Pau Rabassa,² Alef E. Sterk,¹ and Henk Broer²

¹ *College of Engineering, Mathematics and Physical Sciences, University of Exeter, Exeter, UK*

² *Johann Bernoulli Institute for the Mathematical Sciences, Rijksuniversiteit Groningen, Groningen, The Netherlands*

Abstract

Extreme value theory for chaotic deterministic dynamical systems is a rapidly expanding area of research. Given a system and a real function (observable) defined on its phase space, extreme value theory studies the limit probabilistic laws obeyed by large values attained by the observable along orbits of the system. Based on this theory, the so-called block maximum method is often used in applications for statistical prediction of large value occurrences. In this method, one performs statistical inference for the parameters of the Generalised Extreme Value (GEV) distribution, using maxima over blocks of regularly sampled observations along an orbit of the system. The observables studied so far in the theory are expressed as functions of the distance with respect to a point, which is assumed to be a density point of the system's invariant measure. However, this is not the structure of the observables typically encountered in physical applications, such as windspeed or vorticity in atmospheric models. In this paper we consider extreme value limit laws for observables which are not functions of the distance from a density point of the dynamical system. In such cases, the limit laws are no longer determined by the functional form of the observable and the dimension of the invariant measure: they also depend on the specific geometry of the underlying attractor and of the observable's level sets. We present a collection of analytical and numerical results, starting with a toral hyperbolic automorphism as a simple template to illustrate the main ideas. We then formulate our main results for a uniformly hyperbolic system, the solenoid map. We also discuss non-uniformly hyperbolic examples of maps (Hénon and Lozi maps) and of flows (the Lorenz63 and Lorenz84 models). Our purpose is to outline the main ideas and to highlight several serious problems found in the numerical estimation of the limit laws.

*Electronic address: r.vitolo@exeter.ac.uk

Contents

I. Introduction	3
Background on extreme value theory	3
Extremes in deterministic systems	4
Sketch of the results	5
Outline of the paper	6
II. Extremes in dynamical systems: the general problem setting	6
III. A prototypical example: Thom's map	8
A. Analytical calculations	9
B. Numerical results	12
IV. Uniformly hyperbolic attractors: the solenoid map	13
A. Analytical calculations	14
B. Numerical results	16
V. Non-uniformly hyperbolic examples: the Hénon and Lozi maps	18
VI. The Lorenz63 and Lorenz84 flows	22
VII. Discussion and conclusions	26
A. Parameter estimation for the GEV distribution	28
Acknowledgments	29
References	30

I. INTRODUCTION

Background on extreme value theory

Classic extreme value theory concerns the probability distribution of unlikely (large) events, see [2, 8, 10, 13, 24, 37, 43]. Given a stochastic process X_1, X_2, \dots governed by independent identically distributed random variables, let M_n be the random variable defined as the maximum over the first n occurrences:

$$M_n = \max(X_1, \dots, X_n).$$

This variable has a degenerate limit as $n \rightarrow \infty$, and therefore it is necessary to consider a rescaling. Suppose that there exist sequences $a_n \geq 0$ and $b_n \in \mathbb{R}$ such that the rescaled variable $a_n(M_n - b_n)$ converges to a non-degenerate distribution. That is

$$\lim_{n \rightarrow \infty} P(a_n(M_n - b_n) \leq x) = G(x) \quad (1)$$

Then extreme values theory asserts that the limit $G(x)$ can only be one of three different types: the Gumbel, Weibull and Fréchet parametric families of probability distributions. These three families can be combined into a single three-parameter family having distribution function

$$G(x) = \exp \left(- \left[1 + \xi \left(- \frac{x - \mu}{\sigma} \right) \right]^{-1/\xi} \right), \quad (2)$$

defined on the set $\{x \mid 1 + \xi \left(- \frac{x - \mu}{\sigma} \right) > 0\}$, where the parameters satisfy $-\infty < \mu < \infty$, $\sigma > 0$ and $-\infty < \xi < \infty$. Eq. (2) is called the generalised extreme value (GEV) family of distributions. The subset of the GEV family with $\xi = 0$ is interpreted as the limit of (2) as $\xi \rightarrow 0$, leading to the Gumbel family (with parameters μ and σ).

In the applications the GEV family is particularly useful to predict the probability of occurrence of future large values of a quantity, given a sample of past experimental measurements of that quantity. The so-called *block maximum* method is frequently used in this setting. Here one extracts a sub-sample of maxima over data blocks: in environmental and climate contexts one often uses blocks of length one year, hence the name of *annual maximum* method. One then estimates the parameters (μ, σ, ξ) , assuming that that the block maxima form a random sample drawn from a GEV distribution with unknown parameters. Maximum likelihood is a common estimation method [10]: in this case, standard asymptotic theory also provides confidence intervals (uncertainties) for the point estimates. The estimated GEV parameters and associated uncertainties can then

be used to derive other quantities of interest, such as return periods for given return levels of the variable of interest, see the above references and [16, 17, 52, 53] for examples.

Extremes in deterministic systems

Recent work has extended the domain of extreme value theory to the setting of chaotic deterministic dynamical systems [9, 11, 18–22, 27, 29, 31]. We briefly outline the difference of our problem setting as opposed to the above results. Suppose that we have a dynamical system (\mathcal{X}, ν, f) , where \mathcal{X} is a d -dimensional Riemannian manifold, $f : \mathcal{X} \rightarrow \mathcal{X}$ a measurable map and ν an f -invariant probability measure. Assume that there is a compact invariant set $\Lambda \subset \mathcal{X}$ which supports the measure ν . Specifically, our main interest is the situation where Λ is a strange attractor and ν is a Sinai-Ruelle-Bowen (SRB) measure [59]. Given an observable $\phi : \mathcal{X} \rightarrow \mathbb{R} \cup \{+\infty\}$ we study extreme value limit laws for the stationary stochastic process X_1, X_2, \dots defined by

$$X_i = \phi \circ f^{i-1}, \quad i \geq 1. \quad (3)$$

The theoretical work cited above focused on the special case where ϕ has the form

$$\phi(p) = g(\text{dist}(p, p_M)), \quad p \in \mathcal{X}, \quad (4)$$

where $g : [0, +\infty) \rightarrow \mathbb{R}$ is a measurable function of the distance $\text{dist}(\cdot, \cdot)$ in \mathcal{X} and p_M is a density point of ν . However, typical observation functions used in applications *are not of this form*. Consider for example the quasi-geostrophic model of [16, 17]: this model was conjectured in [40] to possess a compact (bounded) strange attractor in its (unbounded) phase space. The observables used in [16, 17, 52, 56] are the system’s total energy, the wind speed and vorticity at a gridpoint in the lower level. These observables can be written as

$$\phi_E(p) = p^T E p, \quad \phi_W(p) = \|W p\|, \quad \phi_V(p) = V p, \quad \text{respectively,} \quad (5)$$

where p is a point in the phase space $\mathcal{X} = \mathbb{R}^d$, $\|\cdot\|$ denotes the Euclidean norm and $E \in \mathbb{R}^{d \times d}$, $W \in \mathbb{R}^{2 \times d}$, $V \in \mathbb{R}^{1 \times d}$ are matrices. None of the observables in (5) has the form (4). In fact this situation is to be expected in many, if not in most, observables found in applications, including the atmospheric and oceanic models of [7, 47]. Although observables such as (5) are usually unbounded in the system’s phase space, the system’s attractor Λ is usually bounded due to the presence of dissipative processes in the models. Therefore, time series of such observables should be expected to have an upper bound

and, hence, large values typically obey Weibull limit distributions, see [16, 52] for a more detailed discussion.

Sketch of the results

In this paper we will consider observables ϕ which are not a function of the distance from a point p_M as in (4). Such observables include cases, like those just mentioned, where ϕ has no upper bound in the phase space, although time series of ϕ on the system's attractor are bounded. Hence we will restrict to the Weibull case in our numerical examples. For comparison with the already available theory, we also consider cases when ϕ is maximised at a point p_M , where however p_M may or may not be a density point for the invariant measure ν .

In such situations, to determine the form of the limiting GEV distribution $G(x)$ becomes a much more delicate problem: $G(x)$ is no longer determined by the functional form of $\phi(p)$ and by the dimension of the SRB measure ν , but also critically depends on the geometry of the attractor $\Lambda \subset \mathcal{X}$ and of the level sets of ϕ . A careful analysis is required even if we assume that ϕ takes the form of (4), but allowing instead that $p_M \notin \Lambda$. Without attempting an exhaustive analysis of all possible cases, we focus on selected examples to illustrate the key ideas of our approach, in view of applications to a given system and observable.

To whet the Reader's appetite, we here anticipate one of the results of this paper. For f we consider the solenoid map [6] embedded in $\mathbb{R}^3 = \{(x, y, z)\}$: this system possesses a strange attractor Λ which is locally the product of a Cantor set with an interval [30], where the interval represent the leaves of a one-dimensional unstable manifold W^u . For the observable we take $\phi(x, y, z) = ax + by + c + d$, which is clearly not of the form (4): rather, ϕ resembles the vorticity observable defined in (5). For this pair of system and observable we obtain the formula

$$-\frac{1}{\xi} = \frac{d_u}{2} + d_s \tag{6}$$

for the tail index ξ of the limiting GEV distribution. Here $d_u = \dim(W^u) = 1$ and d_s is the dimension in the stable direction, which in this case is given by $\dim_H(\Lambda) - 1$, where \dim_H denotes the Hausdorff dimension. Loosely speaking, the factor 1/2 in (6) is obtained under a generic condition of quadratic tangency between a local unstable manifold within the attractor Λ and the level sets of the observable ϕ . As we shall argue, we believe

formula (6) to be valid, or at least sufficiently informative, for a large class of pairs (f, ϕ) of systems-observables. However, we also discuss examples where formula (6) has to be modified to take into account the local geometry or the local scaling of the invariant measure of the attractor, or the local behaviour of the level sets of the observable. We will restrict our discussion to the tail index ξ , which is usually the most delicate parameter to estimate in the analysis of extreme values: see e.g. [2, 10] and [15] for the link between the normalising constants a_n, b_n and the other two GEV parameters μ, σ . We note, however, that our numerical procedure also provides estimates for the latter two parameters, see Appendix A.

Outline of the paper

This paper is organised as follows. The general framework of extremes in dynamical systems is presented in Section II. Our main theoretical results are formulated in Sections III to VI for specific dynamical systems. As a particularly simple example, we consider Thom's map in Section III, to illustrate the main ideas in our approach. Then in Section IV we discuss the solenoid attractor, which displays several features which are found in many concrete physical systems. Section V presents results for two non-uniformly hyperbolic systems, the Hénon and Lozi maps. In Section VI we examine two prototypical flows with chaotic dynamics due to Lorenz [38, 39]. In all of the sections, analytical calculations precede numerical simulations, where the latter aim to show the typical behaviour and estimation problems which can be expected to occur. We return in Section VII to the general relevance of our approach.

II. EXTREMES IN DYNAMICAL SYSTEMS: THE GENERAL PROBLEM SETTING

We consider a measure preserving system (\mathcal{X}, ν, f) with a compact attracting set $\Lambda \subset \mathcal{X}$. Given an observable $\phi : \mathcal{X} \rightarrow \mathbb{R}$ and a threshold $u \in \mathbb{R}$, we define the level regions $L^+(u)$ (resp. level sets $L(u)$) as follows:

$$L^+(u) = \{p \in \mathcal{X} : \phi(p) \geq u\}, \quad L(u) = \{p \in \mathcal{X} : \phi(p) = u\}. \quad (7)$$

For the reasons discussed in the Introduction, we consider observables which achieve a finite maximum within Λ , although the observable themselves could be unbounded in \mathcal{X} .

We define

$$\tilde{u} = \sup_{p \in \Lambda} \phi(p). \quad (8)$$

Since Λ is compact there exists (at least) one point $\tilde{p} \in \Lambda$ for which $\phi(\tilde{p}) = \tilde{u}$. We will assume that such an *extremal point* \tilde{p} is unique. Given our focus on the Weibull case (again, see the Introduction) we consider sequences $u_n = u/a_n + b_n$ for which the limit

$$\lim_{n \rightarrow \infty} n\nu(L^+(u_n)) := \tau(u) \quad (9)$$

exists. From the theory of [36], we can choose $b_n = \tilde{u}$, and we take $a_n \rightarrow \infty$. The precise form of a_n depends on the regularity of ϕ , and the regularity of the density of ν in the vicinity of the extremal point \tilde{p} . In general a_n will be a power law in n , and $\tau(u)$ will be regularly varying in u . If we now consider the process $M_n = \max(X_1, \dots, X_n)$ with $X_n = \phi \circ f^n$, then we investigate to what extent the following statement is true:

$$n\nu\{p : \phi(p) \geq u_n\} \rightarrow \tau(u) \quad \Leftrightarrow \quad \nu\{M_n \leq u_n\} \rightarrow e^{-\tau(u)}. \quad (10)$$

If $\tau(u) = u^\alpha$, then the process M_n is described by a GEV distribution with tail index $\xi = -1/\alpha$. The statement (10) is shown to hold for a wide class of dynamical systems, such as those governed by non-uniformly expanding maps, and systems with (non)-uniformly hyperbolic attractors, [9, 28]. However the current theory for analysing extremes in dynamical systems assumes that the level regions $L^+(u)$ introduced in (7) are described by balls, and moreover that these balls are centred on points in Λ that are generic for ν . These assumptions allow for the tail index to be expressed in terms of local dimension formulae for measures.

In this article we do not assume that the level sets are balls: for example we consider observables of the form $\phi(p) = \phi(x_1, \dots, x_d) = \sum_i |x_i|^{a_i}$, where the level sets have cusps or are non-conformal. We also consider observables $\phi(p) = \sum_i c_i x_i$, for which the level sets are hyperplanes. For observables of these types (also compare with (5)) the standard machinery does not immediately apply. The first problem is to determine the sequence u_n and the limit $\tau(u)$ defined in (9). Even if the measure ν is sufficiently regular then the sequence u_n will depend on the geometry of the attractor close to where $\phi(p)$ achieves its maximum value on Λ , in addition to depending on the form of ϕ . In Section III we illustrate the various geometrical scenarios that can arise using an hyperbolic toral automorphism as a simple example. When ν is a more general SRB measure, then even for uniformly hyperbolic systems (such as the solenoid map) it becomes a non-trivial problem to determine u_n and $\tau(u)$. We discuss this scenario in Section IV. The second problem is to verify statement (10) for the class of observables under consideration. This relies upon

checking two conditions $D_2(u_n), D'(u_n)$, see [19, 28]. We summarise these conditions as follows. For integers t, l let $M_{t,l} = \max\{X_{t+1}, X_{t+2}, \dots, X_{t+l}\}$, with $M_{0,l} := M_l$. Then:

($D_2(u_n)$) We say condition $D_2(u_n)$ holds for the process X_0, X_1, \dots , if for any integers l, t and n we have

$$|\nu(X_1 > u_n, M_{t,l} \leq u_n) - \nu(X_1 > u_n)\nu(M_l \leq u_n)| \leq \gamma(n, t),$$

where $\gamma(n, t)$ is non-increasing in t for each n and $n\gamma(n, t_n) \rightarrow 0$ as $n \rightarrow \infty$ for some sequence $t_n = o(n)$, $t_n \rightarrow \infty$.

($D'(u_n)$) We say condition $D'(u_n)$ holds for the process X_1, X_2, \dots , if

$$\lim_{k \rightarrow \infty} \limsup_{n \rightarrow \infty} n \sum_{l=2}^{\lfloor n/k \rfloor} \nu(X_1 > u_n, X_l > u_n) = 0. \quad (11)$$

If the level sets have complicated geometry, or if the measure ν is supported on a fractal set then these conditions must be carefully checked. For uniformly hyperbolic systems, and for observations that are functions of balls these conditions are checked in [28]. In this article we consider the computation of the GEV tail index ξ for more general observations and contrast to results known for observations that are functions of balls. We focus on particular examples to highlight how the geometrical features of the level sets and the attractor feed into the computation of the tail index ξ , without attempting an exhaustive analysis of all possible cases. We also discuss the computation of the tail index for non-uniformly hyperbolic systems such as the Lozi map and Hénon map, and also for Lorenz flows, again for general observations.

III. A PROTOTYPICAL EXAMPLE: THOM'S MAP

Let $\mathbb{T}^2 = \mathbb{R}^2 \bmod 1$ be the 2 dimensional torus. Thom's map $f : \mathbb{T}^2 \rightarrow \mathbb{T}^2$, also known as *Arnold's cat map*, is the hyperbolic toral automorphism defined by

$$f(x, y) = (2x + y, x + y) \bmod 1. \quad (12)$$

This system is Anosov and it has Lebesgue measure ν on the torus \mathbb{T}^2 as the (unique) invariant measure. With this example we want to study the role of the observable in determining extreme value laws. For this purpose we will consider f as a map of \mathbb{R}^2 having the square $[0, 1]^2$ as the invariant set. In other words, $\mathcal{X} = \mathbb{R}^2$ and $\Lambda = [0, 1]^2$, hence Λ is not an *attractor*, strictly speaking. The advantage is that this allows us to take

functions of \mathbb{R}^2 as observables, rather than functions of \mathbb{T}^2 . In this way, we can construct observables which are maximised at points in the interior or in the complement of Λ and whose level sets have different shapes.

The main point of this section is that the value of the tail index is determined by the interaction between the shape of level sets (7) of the observable and the shape of the support of the invariant measure (colloquially, the geometry of the attractor). To illustrate our ideas, and without attempting to cover all possible cases, we consider the following two observables $\phi_\alpha, \phi_{a,b} : \mathbb{R}^2 \rightarrow \mathbb{R}$

$$\phi_\alpha(x, y) = 1 - \text{dist}(p, p_M)^\alpha, \quad \text{with } p = (x, y) \in \mathbb{R}^2. \quad (13)$$

$$\phi_{a,b}(x, y) = 1 - |x - x_M|^a - |y - y_M|^b, \quad (14)$$

where, given our focus on the Weibull case, we require $a, b, \alpha > 0$. Both observables are maximised at a point $p_M = (x_M, y_M) \in \mathbb{R}^2$. When p_M is in the interior of Λ , observable (13) has the form so far analysed in the mathematical literature about extremes in dynamical systems, but we will also consider the case $p_M \notin \Lambda$. Observable (14) has been chosen to illustrate the effect of the shape of the level sets: the level regions of (14) are not balls unless $a = b = 2$, in which case (14) can be written as (13) for $\alpha = 2$. The next subsection contains our analytical results, numerical simulations are postponed to Section III B.

A. Analytical calculations

The level regions $L^+(u)$ as defined in (7) are always balls for observable (13). However three (main) different situations occur, depending on the location of the point p_M relative to the support of the invariant measure, see the sketch in Figure 1.

Theorem III.1. *Let ξ be the tail index of the GEV limit distribution associated to the process $M_n = \max(X_1, \dots, X_n)$ with $X_n = \phi \circ f^n$, where f is the map (12) and $\phi_\alpha : \mathbb{R}^2 \rightarrow \mathbb{R}$ is the observable in (13). Then for ν -a.e. $p_M = (x_M, y_M) \in \mathbb{R}^2$ we have:*

$$-\frac{1}{\xi} = \frac{2}{\alpha} \quad \text{for } p_M \in \Lambda; \quad (15)$$

$$-\frac{1}{\xi} = \frac{3}{2} \quad \text{for } p_M \notin \Lambda, \text{ with either } y_M \in (0, 1) \text{ or } x_M \in (0, 1); \quad (16)$$

$$-\frac{1}{\xi} = 2 \quad \text{for } p_M \notin \Lambda, \text{ with both } x_M, y_M \notin [0, 1]; \quad (17)$$

For observable (14) the shape of the level sets $L(u)$ depends on a and b . For example, $L(u)$ has a convex elliptic-like shape when both $a, b > 1$ (see the sketch in Figure 2 (A)), or

an asteroid-like shape when both $a, b < 1$, (see Figure 2 (B)). Clearly various possibilities arise, depending on the geometry of the level sets, on whether the point p_M is in the interior of Λ and on the local geometry of Λ near the extremal point $\tilde{p} = (\tilde{x}, \tilde{y})$ with minimum distance from p_M .

Theorem III.2. *Let ξ be the tail index of the GEV limit distribution associated to the process $M_n = \max(X_1, \dots, X_n)$ with $X_n = \phi \circ f^n$, where f is the map (12) and $\phi_{a,b} : \mathbb{R}^2 \rightarrow \mathbb{R}$ is the observable in (14). Then for ν -a.e. $p_M = (x_M, y_M) \in \mathbb{R}^2$ we have:*

$$-\frac{1}{\xi} = \frac{1}{a} + \frac{1}{b} \quad \text{for } p_M \in \Lambda. \quad (18)$$

To prove Theorems III.1-III.2 the main step is to determine the explicit sequence u_n and functional form of $\tau(u)$ as defined in (9). We will not give the verification of $D_2(u_n)$, $D'(u_n)$ as this follows step by step from [28] for this class of observables. The main proof of Theorem III.1 is contained in Lemmas III.3, III.4 and III.5. The proof of Theorem III.2 is given in Lemma III.6. We do not further discuss case (C) of Figure 2, or the other configurations not covered by Figure 2.

Lemma III.3. *Suppose $p_M \in \text{int}(\Lambda) = (0, 1)^2$ and ϕ takes the form of (13), then $\xi = -\alpha/2$.*

Proof. If $p_M \in \text{int}(\Lambda)$ (see Figure 1 (A)), then we see that

$$\begin{aligned} n\nu\{\phi(x, y) \geq u_n\} &= n\nu\{x \leq (1 - u_n)^{1/\alpha}\} \\ &= n(1 - u_n)^{2/\alpha}. \end{aligned} \quad (19)$$

Thus the correct scaling laws are $a_n = n^{\alpha/2}$, $b_n = 1$ and $\tau(u) = (-u)^{2/\alpha}$. \square

Lemma III.4. *Suppose $p_M \notin \bar{\Lambda} = [0, 1]^2$ and ϕ takes the form of (13). If $y_M \in (0, 1)$ or $x_M \in (0, 1)$ then $\xi = -2/3$.*

Proof. If $p_M \notin \bar{\Lambda}$ then there will exist a unique extremal point $\tilde{p} = (\tilde{x}, \tilde{y}) \in \bar{\Lambda}$ where $\phi(p)$ achieves its supremum with value \tilde{u} as in (8). Since $y_M \in (0, 1)$ or $x_M \in (0, 1)$ then this point \tilde{p} will not be a vertex of $\partial\Lambda$, see Figure 1 (B). The scaling u_n will be chosen to so that

$$n\nu\{\phi(x, y) \geq u_n\} = n\nu\{p = (x, y) \in \Lambda : d(p, p_M) \leq (1 - u_n)^{1/\alpha}\} \rightarrow \tau(u). \quad (20)$$

The middle term is no longer $n(1 - u_n)^{1/\alpha}$ since the level region that intersects Λ is not a ball. We first of all set $u_n = u/a_n + \tilde{u}$ so that

$$\nu\{\phi(x, y) \geq u_n\} = \nu\left\{p = (x, y) \in \Lambda : (1 - \tilde{u})^{1/\alpha} \leq d(p, p_M) \leq \left(1 - \tilde{u} - \frac{u}{a_n}\right)^{1/\alpha}\right\}. \quad (21)$$

To choose a_n we first note that the level set $L(\tilde{u}^{1/\alpha})$ as defined in (7) is a circle that is tangent to $\partial\Lambda$ (since the extremal point \tilde{p} is not a vertex). However the level set $L((\tilde{u} - \frac{u}{a_n})^{1/\alpha})$ crosses $\partial\Lambda$ transversally (and is concentric to $L(\tilde{u}^{1/\alpha})$). Thus a basic geometrical calculation gives:

$$\begin{aligned} \nu\{\phi(x, y) \geq u_n\} &= \{(1 - \tilde{u} - u/a_n)^{1/\alpha} - (1 - \tilde{u})^{1/\alpha}\}^{3/2} \\ &= (1 - \tilde{u})^{3/2\alpha} \left\{ \left(1 - \frac{u}{a_n(1 - \tilde{u})}\right)^{1/\alpha} - 1 \right\}^{3/2} \\ &= (1 - \tilde{u})^{3/2\alpha} \left\{ -\frac{u}{\alpha a_n(1 - \tilde{u})} + O\left(\frac{1}{a_n^2}\right) \right\}^{3/2}. \end{aligned} \quad (22)$$

Setting $a_n = n^{2/3}$ implies that $\tau(u) = (-u)^{3/2}$. \square

Lemma III.5. *Suppose $p_M \notin \Lambda$ and ϕ takes the form of (13). If both $x_M, y_M \notin [0, 1]$ then $\xi = -1/2$.*

Proof. Without loss of generality we consider $p_M = (x_M, y_M)$ in the upper right hand quadrant as in Figure 1 (C). Also, we assume that $x_M = 1 + \lambda \cos \theta$, $y_M = 1 + \lambda \sin \theta$ for $\lambda > 0$ and $\theta \in (0, \pi/2)$. For such values of (x_M, y_M) , the corner point $(1, 1) \in \partial\Lambda$ will always maximise ϕ . The proof is identical to Lemma III.4 except that the level sets are not tangent to $\partial\Lambda$ at $(1, 1)$, as illustrated in Figure 1 (C). A simple geometric argument shows that for a disk $D(\epsilon)$ of radius $\lambda + \epsilon$, centred at (x_M, y_M) we have

$$\text{Leb}\{p = (x, y) \in M \cap D(\epsilon)\} = \mathcal{O}(\epsilon^2),$$

where Leb denotes the Lebesgue measure. Setting $u_n = u/a_n + \tilde{u}$ and comparing to (22), we obtain:

$$\begin{aligned} \nu\{\phi(x, y) \geq u_n\} &= \{(1 - \tilde{u} - u/a_n)^{1/\alpha} - (1 - \tilde{u})^{1/\alpha}\}^2 \\ &= (1 - \tilde{u})^{2/\alpha} \left\{ \left(1 - \frac{u}{a_n(1 - \tilde{u})}\right)^{1/\alpha} - 1 \right\}^2 \\ &= (1 - \tilde{u})^{2/\alpha} \left\{ -\frac{u}{\alpha a_n(1 - \tilde{u})} + O\left(\frac{1}{a_n^2}\right) \right\}^2. \end{aligned} \quad (23)$$

Setting $a_n = n^{1/2}$ implies that $\tau(u) = (-u)^2$. \square

This concludes the proof of Theorem III.1. For the proof of Theorem III.2 we have the following lemma.

Lemma III.6. *Suppose that $p_M \in \text{int}(\Lambda) = (0, 1)^2$ and ϕ takes the form of (14). Then for $u \lesssim 1$ we have that $\text{Leb}(L(u)) = C(1 - u)^{\frac{1}{a} + \frac{1}{b}}$ for some $C_0 \leq C \leq 4$ where $C_0 > 0$.*

Proof. Let $u = 1 - \varepsilon$. For ε sufficiently small the level region can be written as

$$L^+(u) = \{(x, y) \in \text{int}(\Lambda) : |x|^a + |y|^b \leq \varepsilon\}. \quad (24)$$

The area of this set is bounded from above by the area of a rectangle of sides $2\varepsilon^{1/a}$ and $2\varepsilon^{1/b}$. Also, for any $q \in (0, 1)$, the area of the set is bounded from below by that of a rectangle of sides $2q^{1/a}\varepsilon^{1/a}$ and $2(1 - q)^{1/b}\varepsilon^{1/b}$, so we can choose $C_0 = 4q^{1/a}(1 - q)^{1/b}$. \square

Hence if $(x_M, y_M) \in \text{int}(\Lambda)$, we see that

$$n\nu\{p = (x, y) : \phi(p) \geq u_n\} \rightarrow (-u)^{\frac{1}{a} + \frac{1}{b}} \quad \text{with} \quad a_n = n^{\frac{ab}{a+b}}, b_n = 1. \quad (25)$$

B. Numerical results

As formula (18) shows, one of the main ingredients in determining the tail index is the shape of the level sets of the observable. We here fix $a = 2$ and consider two values of b , namely $b = 1$ and $b = 3.5$. In both cases, the value of ξ expected according to (18) is less than -0.5 . Since the maximum likelihood estimator is not regular for $\xi < -0.5$ [10], we resort to the method of L-moments for the numerical estimation of the GEV parameters. See Appendix A for details on our procedure for parameter estimation and associated uncertainties.

In Figure 3 we examine the sensitivity of the numerical estimates of ξ with respect to the block length used to compute the maxima. Essentially no significant variations are found for block lengths larger than 1000. Hence, we fix $N_{blocklen} = 10000$ and conduct a study of the dependence of the tail index on the parameter b of the observable (18). Figure 4 shows a good agreement with the theoretical predictions of (18) for a range of values of b . In this example the level regions of the observable of the form $L^+(u)$ as in (7) are fully contained in the interior of $\Lambda = [0, 1]^2$, at least for sufficiently large values of the threshold u . The only peculiarity is the non-circular shape of $L^+(u)$, see Figure 2 and compare with Lemma III.6.

We now consider a case where the level regions $L^+(u)$ are not fully contained in Λ . We take observable (13) and vary the location of the point $p_M = (x_M, y_M)$. Starting from values x_M, y_M such that p_M is in the interior of Λ we increase x_M across 1, bringing p_M in the region where $y_M \in (0, 1)$ but $x_M \notin (0, 1)$. This transition is illustrated in panels (A) and (B) of Figure 1 and the two situations correspond to (15) and (16) respectively.

Figure 5 shows the sensitivity of the numerical estimates of ξ with respect to the block length used to compute the maxima for four values of x_M . Convergence to the theoretical value (15) is achieved already with block lengths of a few hundred iterates when the point p_M is in the interior of Λ (panel (A), $x_M = 0.9$) and on the boundary of Λ (panel (B), $x_M = 1.0$). When p_M is in the complement of $\bar{\Lambda} = [0, 1]^2$ but close to its boundary, then very large block lengths ($N_{blocklen} > 10^5$) are required to achieve convergence to the theoretical value of (16) (panel (C), $x_M = 1.01$). When p_M is further away from $[0, 1]^2$ shorter block lengths of about 10^4 iterates already guarantee convergence to the theoretical value of (16) (panel (D), $x_M = 1.1$).

Figure 6 (A) shows the discontinuity of ξ in the transition between the situations of panels (A) and (B) in Figure 1. The figure shows the estimated value of ξ as a function of x_M where y_M is kept constant and a fixed block length is used. As the point p_M exits Λ , the value of ξ has a jump from the value of (15) to that of (16). However, the numerical estimation does not resolve this jump unless large block lengths ($N_{blocklen} > 10^5$ iterates) are used.

Lastly, Figure 6 shows the discontinuity of ξ from (16) to (17), at the transition between the situations of panels (B) and (C) in Figure 1. This transition is not resolved accurately even with block lengths of 10^5 . From the numerical point of view, very large block lengths are required near the transition to detect the change of scaling between (22) and (23).

The example discussed in this section is admittedly somewhat artificial. It has been chosen to clearly illustrate the main ideas and the problems which are found in the numerical estimation, without the additional complications due to higher dimensionality of phase space and fractal nature of the attractors. In the next section, we consider a situation which is closer to what one can expect in concrete physical systems.

IV. UNIFORMLY HYPERBOLIC ATTRACTORS: THE SOLENOID MAP

Consider the solid torus as the product of $\mathbb{T} = \mathbb{R}/\mathbb{Z}$ times the unit disc in the complex plane $\mathbb{D}_R = \{z \in \mathbb{C} \mid |z| < 1\}$. Then the solenoid map is defined as follows:

$$\begin{aligned}
 f_\lambda : \mathbb{T} \times \mathbb{D} &\rightarrow \mathbb{T} \times \mathbb{D} \\
 (\psi, w) &\mapsto (2\psi, \lambda w + K e^{i2\pi\psi}).
 \end{aligned}
 \tag{26}$$

In order to have the map well defined we need $K + \lambda R < R$ and $\lambda R < K$. For our purposes it is convenient to have the torus embedded in \mathbb{R}^3 . Consider Cartesian

coordinates $(x, y, z) \in \mathbb{R}^3$ and define corresponding cylindrical coordinates r, ψ, z by $x = r \cos(\psi)$ and $y = r \sin(\psi)$. Then the torus of width R can be identified with the set $D = \{(r-1)^2 + z^2 \leq R^2\}$ for $R < 1$. The torus $\mathbb{T} \times \mathbb{D}_R$ (with coordinates $(\psi, u + iv)$) can be identified with D taking $r = 1 + u$ and $z = v$. We thus obtain an embedded solenoid map

$$g_\lambda : D \rightarrow D, \quad g_\lambda(\psi, r, z) = (2\psi, 1 + K \cos(\psi) + \lambda(r-1), K \sin(\psi) + \lambda z). \quad (27)$$

The solenoid attractor is defined as the attracting set of the map g_λ :

$$\Lambda = \bigcap_{j \geq 1} g_\lambda^j(D).$$

For $\lambda < \frac{1}{2}$ we have

$$\dim_H(\Lambda) = 1 + \frac{\log 2}{\log \lambda^{-1}}, \quad (28)$$

where \dim_H denotes the Hausdorff dimension [45]. We consider the following observables $\phi_\alpha, \phi_{abcd} : \mathbb{R}^3 \rightarrow \mathbb{R}$:

$$\phi_\alpha(x, y, z) = 1 - \text{dist}(p, p_M)^\alpha, \quad \text{with } p = (x, y, z) \in \mathbb{R}^3, \quad (29)$$

$$\phi_{abcd}(x, y, z) = ax + by + cz + d, \quad (30)$$

Observable (29) is maximised at a point $p_M \in \mathbb{R}^3$, whereas (30) is unbounded in the phase space \mathbb{R}^3 (except for the trivial choice $a = b = c = 0$). Note that the vorticity observable ϕ_V of (5) has the same general form as (30). Our theoretical expectations are first discussed in Section IV A, followed by numerical results in Section IV B.

A. Analytical calculations

For observables which are functions of distance we have the following result. It is not explicitly stated in the literature but the proof follows straightforwardly from [28].

Theorem IV.1. *Let ξ be the tail index of the GEV limit distribution associated to the process $M_n = \max(X_1, \dots, X_n)$ with $X_n = \phi \circ g_\lambda^n$, where g_λ is the map (27) and $\phi_\alpha : \mathbb{R}^3 \rightarrow \mathbb{R}$ the observable of (29), where $p_M \in \Lambda$. Then we have:*

$$-\frac{1}{\xi} = \frac{\dim_H(\Lambda)}{\alpha}. \quad (31)$$

More interesting considerations arise for the observable (30). As a simple case, consider first the degenerate solenoid with $\lambda = 0$ and take a planar observable $\phi := ax + by + d$,

thus reducing the problem to the (x, y) -plane. In this case we have the trivial dimension formula $\dim_H(\Lambda) = 1$ since Λ is a circle. However, for computing the tail index we lose a factor of $1/2$ due to the geometry of the level set. Indeed, level sets are straight lines within the (x, y) -plane, and at the extremal point $\tilde{p} = (\tilde{x}, \tilde{y})$ the critical level set $L(\tilde{u})$ is tangent to Λ . Since the tangency is quadratic, we find that

$$\nu(L^+(\tilde{u} - \epsilon)) = m_{\gamma^u}\{\gamma^u(\tilde{p}) \cap L^+(\tilde{u} - \epsilon)\} = \mathcal{O}(\sqrt{\epsilon}). \quad (32)$$

Here $\gamma^u(\tilde{p})$ is the unstable manifold through \tilde{p} (i.e. it is the unit circle), and m_{γ^u} is the one-dimensional conditional (Lebesgue) measure on $\gamma^u(\tilde{p})$. Hence

$$-\frac{1}{\xi} = \dim_H(\Lambda) - \frac{1}{2} = \frac{1}{2}.$$

The mechanism described above is similar to that illustrated for Thom's map in Figure 1 (B), leading to formula (16): indeed, there we have $\dim_H(\Lambda) = 2$, yielding the value $3/2$ for the tail $-1/\xi$.

For $\lambda > 0$, the attractor has more complicated geometry and is locally the product of a Cantor set with an interval [30]. Planar cross sections that intersect Λ transversely form a Cantor set of dimension $\dim_H(\Lambda) - 1 = -\log 2 / \log \lambda$. To calculate $\nu(L^+(\tilde{u} - \epsilon))$ we would like to repeat the calculation above using equation (32), but now the set of unstable leaves that intersect $L^+(\tilde{u} - \epsilon)$ form a Cantor set (for each $\epsilon > 0$). The extremal point \tilde{p} where $\phi(p)$ attains its maximum on Λ forms a *tip* of Λ relative to $L(\tilde{u})$. Such a tip corresponds to a point on $\tilde{p} \in \Lambda$ whose unstable segment $\gamma^u(\tilde{p})$ is tangent to $L(\tilde{u})$ at \tilde{p} , and moreover normal to $\nabla\phi(\tilde{p})$ at \tilde{p} . Given $\epsilon > 0$, we (typically) expect to find a Cantor set of values $t \in [0, \epsilon]$ for which the level sets $L(\tilde{u} - t)$ are tangent to some unstable segment $\gamma^u \subset \Lambda$. For other values of t these level sets cross the attractor transversally. Given (fixed) $\epsilon_0 > 0$ we can define the *tip set* $\Gamma \equiv \Gamma(\epsilon_0) \subset \Lambda$ as follows: let $T_p\gamma^u(p)$ be the tangent space to γ^u at p . Then we define

$$\Gamma = \{p \in L^+(\tilde{u} - \epsilon_0) \cap \Lambda : T_p\gamma^u(p) \cdot \nabla\phi(p) = 0\}. \quad (33)$$

This tip set plays a role in proving the following result, which in turn provides us with information on the form of the tail index ξ .

Proposition IV.2. *Suppose that g_λ is the map (27) and $\phi = \phi_{abcd}$. Define $\tau(\epsilon) = \nu\{\phi(p) \geq \tilde{u} - \epsilon\}$. If $\dim_H(\Gamma) < 1$, then modulo a zero measure set of values (a, b, c, d) , $\tau(\epsilon)$ is regularly varying with index $1/2 + \dim_H(\Gamma)$ as $\epsilon \rightarrow 0$.*

We give a proof below. Based on this proposition we conjecture that

$$-\frac{1}{\xi} = \dim_H(\Lambda) - \frac{1}{2} = \frac{1}{2} + \frac{\log 2}{\log \lambda^{-1}}. \quad (34)$$

We outline the main technical challenges that would need to be overcome to prove this conjecture. Firstly, conditions $D(u_n)$ and $D'(u_n)$ should be checked. We believe that this should follow from [28], however the proof would be non-standard due to the level set geometry. Secondly, we would claim that $\dim_H(\Gamma) = \dim_H(\Lambda) - 1$. The proof of this would utilise the techniques used in [30] to analyse the regularity of the holonomy map between stable disks. In particular, the Authors of [30] show that the holonomy map is Lipschitz on a set of full dimension. However, it does not automatically follow that the holonomy map between Γ and $\Lambda \cap D$ is Lipschitz (for a disk D transverse of Λ), but we believe that it is for general planar observations.

Proof of Proposition IV.2. For each $\epsilon < \epsilon_0$, consider the set $\Gamma(\epsilon) \subset \Gamma \cap L^+(\tilde{u} - \epsilon)$. Then for each $p \in \Gamma(\epsilon)$, there exists $t < \epsilon$ such that $\gamma^u(p)$ is tangent to $L(\tilde{u} - t)$. If the observable ϕ takes the form of (30), then by the same calculation as (32) we obtain

$$m_{\gamma^u}\{\gamma^u(p) \cap L^+(\tilde{u} - \epsilon)\} = \mathcal{O}(\sqrt{\epsilon - t}). \quad (35)$$

Thus to compute $\nu(L^+(\tilde{u} - \epsilon))$, we integrate (35) over all relevant $t < \epsilon$ using the measure ν_Γ , which is the measure ν conditioned on Γ . Provided $\dim_H(\Gamma) < 1$, the projection of Γ onto the line in the direction of $\nabla\phi$ is also a Cantor set of the same dimension for typical (full volume measure) (a, b, c, d) , see [14]. Thus the set of values t corresponding to when $L(\tilde{u} - t)$ is tangent to Γ form a Cantor set of dimension $\dim_H(\Gamma)$. If π is the projection from Γ onto a line in the direction of $\nabla\phi$, then the projected measure $\pi_*\nu_\Gamma$ has local dimension $\dim_H(\Gamma)$ for typical (a, b, c, d) . We have

$$\nu(L^+(\tilde{u} - \epsilon)) = \int_0^\epsilon \int_{L^+(\tilde{u}-\epsilon)} dm_{\gamma^u} d\nu_\Gamma. \quad (36)$$

To estimate this integral we bound it above via the inequality $m_{\gamma^u}(\gamma^u \cap L^+(\tilde{u} - \epsilon)) \leq C\sqrt{\epsilon}$, and bound it below using the fact that for $t > \epsilon/2$, $m_{\gamma^u}(\gamma^u \cap L^+(\tilde{u} - \epsilon)) \geq C\sqrt{\epsilon}$. Here $C > 0$ is a uniform constant. Putting this together we obtain for typical (a, b, c, d)

$$\nu(L^+(\tilde{u} - \epsilon)) = \int_0^\epsilon \int_{L^+(\tilde{u}-\epsilon)} dm_{\gamma^u} d\nu_\Gamma \approx \sqrt{\epsilon} \cdot \epsilon^{\dim_H(\Gamma)} = \epsilon^{1/2 + \dim_H(\Gamma)}. \quad (37)$$

□

B. Numerical results

We now examine the convergence of the numerically estimated values to the theoretically expected ones. For the numerical simulations, we rewrite observable (30) in two forms

$\phi_{\theta,1}, \phi_{\theta,2} : \mathbb{R}^3 \rightarrow \mathbb{R}$ (form (30) is recovered for suitable values of a, b, c, d):

$$\phi_{\theta,1}(x, y, z) = \cos(2\pi\theta)(x - x_0) + \sin(2\pi\theta)(y - y_0), \quad (38)$$

$$\phi_{\theta,2}(x, y, z) = \cos(2\pi\theta)(x - x_0) + \sin(2\pi\theta)(z - z_0). \quad (39)$$

The level sets associated to (38) and (39) are planes orthogonal to $(\cos(2\pi\theta), \sin(2\pi\theta), 0)$ and $(\cos(2\pi\theta), 0, \sin(2\pi\theta))$, respectively. Figure 7 shows the dependence of the estimates of ξ with respect to the block length $N_{blocklen}$ for both (38) and (39) at $\theta = 0.5$. Figure 7 suggests that the block length $N_{blocklen} = 10^4$ is sufficient to get an estimate coherent with the theoretical value (34) for observable (38), whereas the same value is not sufficient for observable (39). This is illustrated in Figure 8 for a range of values of θ : reliable estimation is obtained with block length $N_{blocklen} = 10^4$ for observable (38) (panel (A)) but not for observable (39) (panel (B)), for which $N_{blocklen} = 10^6$ seems to suffice (panel (C)).

In summary, the minimum block length required for (approximate) convergence to the theoretical value may vary strongly with the location within the attractor of the extremal point \tilde{p} in (32), that is with the relative position of the attractor and the level sets. Also, the minimum block length may depend on the dimensionality of the attractor. Numerical experiments suggest that reliable estimation is more difficult when the dimensionality of the attractor is smaller. Figure 9 indeed shows better agreement with the prediction of (34) for the larger values of λ which also correspond to a larger dimension according to (28).

Lastly, we consider observable (29). As we did in Figure 5, we illustrate the effect of the point p_M “dropping out” of the attractor Λ . To achieve this, we iterate the solenoid map starting from an arbitrarily chosen initial condition. After discarding a transient of 10^5 iterates, we regard the final point p_M^0 of the orbit as being generic with respect to the Sinai-Ruelle-Bowen measure on Λ . Figure 10 (A) shows the sensitivity of the estimates of ξ with respect to block length for observable (29) when p_M is equal to p_M^0 as obtained above. The estimates display strong oscillations around the theoretical value and barely seem to settle for very large block lengths $N_{blocklen} > 10^7$. We return to this problem in Section V.

We then choose p_M as a perturbation of point p_M^0 in the radial direction in \mathbb{R}^3 : namely we set $p_M = p_M^t = (1 + t)p_M^0$. By dissipativity of the solenoid map, we expect $p_M^t \notin \Lambda$ with probability 1 when $t \neq 0$. We find out that when t is sufficiently large (Figure 10 B)), the estimates of ξ converge to the theoretically expected value (34) already for block lengths of 1000. However, when t is small (Figure 10 C)) the estimates are closer to the value

attained within the attractor (31) for small block lengths, whereas convergence to the theoretically expected value (34) takes place for $N_{blocklen}$ larger than about 10^5 .

V. NON-UNIFORMLY HYPERBOLIC EXAMPLES: THE HÉNON AND LOZI MAPS

We here consider the Hénon map [3, 9]

$$h_{a,b} : \mathbb{R}^2 \rightarrow \mathbb{R}^2, \quad h_{a,b}(x, y) = (1 - ax^2 + y, bx), \quad (40)$$

for the classical parameter values $(a, b) = (1.4, 0.3)$ and the Lozi map [12, 58]

$$l_{a,b} : \mathbb{R}^2 \rightarrow \mathbb{R}^2, \quad l_{a,b}(x, y) = (1 - a|x| + y, bx), \quad (41)$$

for $(a, b) = (1.7, 0.1)$, under the observables

$$\phi_\alpha(x, y) = -\text{dist}(p, p_M)^\alpha, \quad \text{with } p = (x, y) \in \mathbb{R}^2, \quad (42)$$

$$\phi_\theta(x, y) = x \cos(2\pi\theta) + y \sin(2\pi\theta), \quad (43)$$

where $\alpha > 0$ and $\theta \in [0, 2\pi]$ are parameters and p_M is a point in \mathbb{R}^2 . Following the discussion for the solenoid map, we could conjecture that

$$-\frac{1}{\xi} = \frac{\dim_H(\Lambda)}{\alpha} \quad \text{for } \phi = \phi_\alpha \text{ and } p_M \in \Lambda; \quad (44)$$

$$-\frac{1}{\xi} = \dim_H(\Lambda) - \frac{1}{2} \quad \text{for } \phi = \phi_\theta. \quad (45)$$

The numerical verification of these conjectures turns out to be rather problematic. First of all for a given system it may be very hard or even unfeasible to compute an estimate of the Hausdorff dimension. For this reason, we will use the Lyapunov (Kaplan-Yorke) dimension of the Hénon or Lozi attractor instead of the Hausdorff dimension appearing in (45)-(44). The Lyapunov dimension of an attractor $\Lambda \subset \mathbb{R}^n$ of a system with \mathbb{R}^n as phase space is defined as

$$\dim_L(\Lambda) = k + \frac{\sum_{j=1}^k \chi_j}{-\chi_{k+1}}, \quad (46)$$

where $\chi_1 \geq \chi_2 \geq \dots \geq \chi_n$ are the Lyapunov exponents and k is the maximum index for which $\sum_{j=1}^k \chi_j \geq 0$. It is believed that the Lyapunov dimension forms an upper bound for the Hausdorff dimension under general conditions [26, 35].

For the Hénon map under observable (13), and in view of the results of a recent paper [9], it is expected that formula (44) holds for so-called *Benedicks-Carleson parameter*

values [23]. Such parameter values, however, are obtained by a perturbative argument near $(a, b) = (2, 0)$, where the bound on the smallness of b is not explicit. Moreover, the parameter exclusion methods used to define the Benedicks-Carleson parameter values are not constructive. For these reasons, it is not possible to say whether Benedicks-Carleson behaviour is also attained at the “classical” parameter values $(a, b) = (1.4, 0.3)$. Despite this, (44) forms our best guess for the value of ξ .

For planar observables, we again study the *tip set* $\Gamma \subset \Lambda$ as defined for the Solenoid map, namely, for fixed $\epsilon_0 > 0$ and $p = (x, y)$, let

$$\Gamma = \{p \in L^+(\tilde{u} - \epsilon_0) \cap \Lambda : T_p \gamma^u(p) \cdot \nabla \phi(p) = 0\}, \quad (47)$$

and for each $\epsilon < \epsilon_0$, consider the set $\Gamma(\epsilon) \subset \Gamma \cap L^+(\tilde{u} - \epsilon)$. Then for each $p \in \Gamma(\epsilon)$, there exists $t < \epsilon$ such that $\gamma^u(p)$ is tangent to $L^+(\tilde{u} - t)$. For the planar observable ϕ we would expect to obtain (as with the solenoid):

$$m_{\gamma^u} \{\gamma^u(p) \cap L^+(\tilde{u} - \epsilon)\} = \mathcal{O}(\sqrt{\epsilon - t}), \quad (48)$$

where m_{γ^u} is the conditional (Lebesgue) measure on the one-dimensional unstable manifold. However in this calculation we have assumed that the tangency between $\gamma^u(p)$ and $L(\tilde{u} - t)$ is quadratic, and that the unstable segment is sufficiently long so as to cross $L(\tilde{u} - \epsilon)$ from end to end. For the Hénon map both of these conditions can fail. In particular, the Hénon attractor admits a critical set of folds that correspond to points where the attractor curvature is large. More precisely the critical set is formed by homoclinic tangency points between stable and unstable manifolds. This set has zero measure, but it is dense in the attractor. Furthermore the attractor has complicated geometry, where local stable/unstable manifolds can fold back and forth upon themselves. However, the regions that correspond to these folds (of high curvature) occupy a set of small measure. See [57] and references therein for a more detailed discussion.

To compute the tail index, we conjecture to have the following formula:

$$-\frac{1}{\xi} = \dim_H(\nu) - \frac{1}{2} \quad (49)$$

where ν is the SRB measure for the Hénon map (at Benedicks-Carleson parameters). This would follow from the estimate:

$$\nu(L^+(\tilde{u} - \epsilon)) = \int_0^\epsilon \int_{L^+(\tilde{u} - \epsilon)} dm_{\gamma^u} d\nu_\Gamma \approx \sqrt{\epsilon} \cdot \epsilon^{\dim_H(\Gamma)}, \quad (50)$$

where the factor of $\sqrt{\epsilon}$ comes from equation (35). To obtain equation (49), we would need to show that $\dim_H(\Gamma) = \dim_H(\nu) - 1$. This is perhaps harder to verify and it will

depend on the regularity of the holonomy map taken along unstable leaves. Finally we would project this set onto a line in the direction of $\nabla\phi(p)$, and typically the projection would preserve the dimension.

Figure 11 shows the dependence of the estimates of ξ with respect to the block length $N_{blocklen}$ for the Hénon map under the observable (13). We see that the estimates exhibit strong oscillations around the value predicted by (44) even for fairly large block lengths. Figure 12 shows the dependence of the estimates of ξ with respect to the block length $N_{blocklen}$ for the Hénon map under the observables (43) at $\theta = 0, 0.5$. The horizontal lines represent the values predicted by (45), where, as above, we have used the of Lyapunov (Kaplan-Yorke) dimension of the Hénon attractor instead of the Hausdorff dimension. We see that block lengths of at least 10^4 are required for the estimation to reach the neighbourhood of the value predicted by (45). However, the estimates still exhibit substantial oscillations around the predicted values for block lengths as large as 10^7 , although both the variability of the individual point estimates and the estimation uncertainty are here much less pronounced than in Figure 11.

We had already seen the above behaviour in the solenoid map: namely, the estimates in panel (A) of Figure 10 also exhibit larger variance and variability than those in panel (C). In that case, however, the theoretical value of panel (A) is not conjectural, since it follows from the theory discussed in Section IV for observables such as (29) when the point p_M belongs to the attractor.

Hence we do not interpret the variability in Figures 11 and 12 as a dismissal of (45)-(44). Rather, we claim that this behaviour is due to a problematic aspect of the numerical estimation. To illustrate our claim, we more carefully examine the estimates of the GEV distribution obtained for block lengths of 5000 and 10000, for observable (43) with $\theta = 0$. In this case, the observable simply coincides with the projection on the x -axis: this is very useful for the visualisation.

The kernel-smoothed density of the block maxima show various peaks (panel (A1) in Figure 13). A particularly pronounced peak occurs nearby $x = 1.2727$. Examination of the points on the time series of the block maxima (panel (B1)) and of the points on the Hénon attractor corresponding to the block maxima (panel (C1)) reveals that this peak is associated to a pair of branches of the attractor that exhibit a turning point slightly above 1.2727. This peak corresponds to a “corner” in the quantile-quantile plot (panel (D1)) comparing the empirical distribution of the block maxima to fitted GEV distribution. For values of x at the left of the peak, the empirical distribution of the block

maxima displays a strong deviation from the fitted GEV distribution.

When the block length is increased to 10^4 (right column of Figure 13), the kernel-smoothed density of the block maxima drops to almost zero at the left of the peak (panel (A2)). Indeed, the portion of the Hénon attractor corresponding to the block maxima (panel (C2)) does *no longer* include the two leftmost branches which were found in panel (C1). Moreover, a much smaller fraction of points now belongs to the branch of the attractor having a turning point at 1.2727. This also corresponds to the peak in the density being lower in panel (A2) than in panel (A1). More importantly, this correspond to a much better overall fit to the GEV distribution: as illustrated by the quantile-quantile plot in panel (D2), there still is some deviation at the lower tail, but it is orders of magnitude smaller than in panel (D1).

We believe that this is the explanation for the poor convergence to the theoretical estimates which we have found in Figure 12, also see [42] for a related discussion. The fractal structure portrayed in panels (D1-2) of Figure 13 is indeed present at all spatial scales near the extremal point $\tilde{p} = (\tilde{x}, \tilde{y})$ on the Hénon attractor for which observable (43) with $\theta = 0$ is maximised. As blocks of increasing lengths are used, increasingly many attractor branches are discarded. Near the block length values for which one major branch is discarded, a better agreement is obtained between the sample of block maxima and the limiting GEV distribution. These are the block length values for which we expect the estimated value of ξ to lie closer to the theoretical prediction in panel (A) of Figure 12.

The effect of the variability in the estimates is illustrated in Figure 14, where we show estimates of ξ for observable (45) with several values of θ and with four block lengths. For $N_{blocklen} = 10^3$, the estimates vary substantially across the range of values of θ (Figure 14 (A)). Varying θ from 0 to 1 amounts to rotate the level sets of the observable (45), which are straight lines. Hence, this amounts to slide the extremal point \tilde{p} for which observable (43) is maximised on the Hénon attractor (compare with (7)). The horizontal *plateau* in Figure 14 (A), occurring approximately for θ between $[0.5, 0.75]$, corresponds to the extremal point \tilde{p} belonging to the leftmost tip-like portions of the Hénon attractor: large variations in θ in this range correspond to small variations in \tilde{p} .

For block lengths of $N_{blocklen} = 10^4$, (Figure 14 (B)), the estimates are more uniform across θ . The same holds for $N_{blocklen} = 10^5$ and 10^6 and we see a definite bias in the latter case, which has the same sign and approximately the same value for all θ . Roughly speaking, choosing block lengths of at least $N_{blocklen} = 10^4$ ensures that we only select block maxima in branches of the Hénon attractor which are close to its outer “peel”,

compare with Figure 13 (C1-C2). However, this does not necessarily guarantee accurate estimation of the limit value of ξ , for the reason illustrated in Figure 13 (D1-D2).

We argue that the same explanation holds for the variability of the estimates in panel (A) of Figure 10 and for the even poorer convergence in Figure 11. Plots similar to Figure 13 for the latter case suggest that as block length is increased, the probability mass that is lost at the lower tail of the empirical distribution of the block maxima is redistributed amongst other attractor branches which lie closer to the point p_M^0 . To illustrate this process we chose observable (43) for ease of visualisation.

Similar considerations hold for the Lozi map (41). Figure 15 shows the sensitivity of the numerical estimates of ξ with respect to the block length used to compute the maxima for observable (42). For the chosen parameter values, we obtain the estimate $\dim_L(\Lambda) = 1.185$, in good agreement with the bounds $1.176669 < \dim_H(\Lambda) < 1.247848$ on the Hausdorff dimension of the Lozi attractor Λ proved in [34]. When the point p_M is chosen in the attractor of the Lozi map, the estimates display strong oscillations around the value predicted by the theory (Figure 15 panel (A)), as in Figure 11. We then choose $p_M = (0.2, 0.01)$: this point does not lie on the attractor of the Lozi map, but the nearest point (\tilde{x}, \tilde{y}) on the attractor belongs to one of the straight portions. Also in this case we observe oscillations around the theoretically expected value (Figure 15 panel (B)), like in Figure 12.

VI. THE LORENZ63 AND LORENZ84 FLOWS

The theoretical and numerical machinery developed in the previous sections is now applied to two paradigmatic ordinary differential equations, both derived and studied by Ed Lorenz. We first of all consider the model of [38]:

$$\begin{aligned}\dot{x} &= \sigma(y - x), \\ \dot{y} &= x(\rho - z) - y, \\ \dot{z} &= xy - \beta z,\end{aligned}\tag{51}$$

derived from the Rayleigh equations for convection in a fluid layer between two plates. Here σ is the Prandtl and ρ the Rayleigh number. We refer to this as the Lorenz63 model and fix $\sigma = 10$, $\beta = 8/3$ and $\rho = 28$, which is a fairly common choice in the vast literature on the Lorenz63 system, see e.g. [1, 46, 48]. The statistics of extremes has been previously analysed in [52], who found smooth-like variation of the GEV parameters with respect to

changes in the parameter ρ within a suitable range.

We also study a three-dimensional system proposed by Lorenz in 1984 [39]:

$$\begin{aligned}\dot{x} &= -ax - y^2 - z^2 + aF, \\ \dot{y} &= -y + xy - bxz + G, \\ \dot{z} &= -z + bxy + xz.\end{aligned}\tag{52}$$

This is derived by a Galerkin projection from an infinite dimensional model for the atmospheric circulation at mid-latitudes in the Northern Hemisphere. The variable x is the strength of the symmetric, globally averaged westerly wind current. The variables y and z are the strength of cosine and sine phases of a chain of superposed waves transporting heat poleward. The terms in b represent displacement of the waves due to interaction with the westerly wind. The coefficient a , if less than one, allows the westerly wind current to damp less rapidly than the waves. The time scale of t corresponds to about 5 days. The terms in F and G are thermal forcings: F represents the *symmetric* cross-latitude heating contrast and G accounts for the *asymmetric* heating contrast between oceans and continents. System (52) has been used in both climatological studies, for example by coupling it with a low-dimensional model for ocean dynamics [50]. Several works have examined its bifurcations, mainly in the (F, G) -parameter plane [4, 41, 44, 49]. Almost nothing is known theoretically regarding the structure of its strange attractors. As in the above references, we fix $a = 0.25$ and $b = 4$ and consider the chaotic dynamics occurring at $(F, G) = (8, 1)$.

We analyse time series generated by observables computed along orbits of these flows, sampled every Δt time units. We fix $\Delta t = 0.05$ time units for the Lorenz63 and $\Delta t = 0.1$ for the Lorenz84 model. We consider the two observables

$$\phi_1(x, y) = -\text{dist}(p, p_M), \quad \text{with } p = (x, y, z) \in \mathbb{R}^3,\tag{53}$$

$$\phi_2(x, y, z) = x.\tag{54}$$

Observable ϕ_2 has a clear physical meaning in both models: for (51), the variable x represents the intensity of the convection, whereas in (52) the variable x represents the strength of the westerly wind current. As in the previous sections, we examine the sensitivity of the numerical estimates of ξ with respect to the block length used to compute the maxima.

We first consider the Lorenz63 system (51). It will be useful to recall some geometrical facts of the Poincaré map to $z = \text{constant}$ sections. Given the planar sections $\Sigma = \{(x, y, 1) : |x|, |y| \leq 1\}$, and $\Sigma' = \{(1, y, z) : |y|, |z| \leq 1\}$, the map $P : \Sigma \rightarrow \Sigma$ decomposes

as $P = P_2 \circ P_1$, where $P_1 : \Sigma \rightarrow \Sigma'$ and $P_2 : \Sigma' \rightarrow \Sigma$. To describe the form of P , let $\beta = |\lambda_s|/\lambda_u$, $\beta' = |\lambda_{ss}|/\lambda_u$, where λ_s , λ_{ss} and λ_u are the eigenvalues of the linearised Lorenz63 flow at the origin, with $\lambda_s = -8/3$, $\lambda_{ss} = -22.83$ and $\lambda_u = 11.83$ for our choice of parameters. Then it can be shown that $P_1(x, y, 1) = (1, x^{\beta'}y, x^\beta)$, and P_2 is a diffeomorphism, see [32]. Thus the rectangle $\Sigma^+ = \{(x, y, 1) : x > 0, |y| \leq 1\}$ gets mapped into a region $P_1(\Sigma^+)$ with a cusp at $y = 0$. The cusp boundary can be represented as the graph $|y| = z^{\beta'/\beta} \approx z^8$. The flow has a strong stable foliation, and we form the quotient space $\widehat{\Sigma} = \Sigma / \sim$ by defining an equivalence relation $p \sim q$ if $p \in \gamma^s(q)$, for a stable leave γ^s . Hence the map $P : \Sigma \rightarrow \Sigma$ can be reduced to a uniformly expanding one-dimensional map $f : \widehat{\Sigma} \rightarrow \widehat{\Sigma}$, with a derivative singularity at $x = 0$. Here $\widehat{\Sigma}$ identified with $[-1, 1]$, and $f'(x) \approx |x|^{\beta-1}$ near $x = 0$.

The Lorenz flow admits an SRB measure ν which can be written as $\nu = \nu_P \times \text{Leb}$ (up to a normalisation constant). The measure ν_P is the SRB measure associated to the Poincaré map P , and the measure is exact dimensional, i.e. the local dimension is defined ν -a.e., see [25]. Using the existence of the stable foliation, and the SRB property of ν , we can write ν_P as the (local) product $\nu_{\gamma^u} \times \nu_{\gamma^s}$ where ν_{γ^u} is the conditional measure on unstable manifolds, and ν_{γ^s} is the conditional measure on stable manifolds. We can identify each measure ν_{γ^u} (via a holonomy map) with that of the invariant measure ν_f associated to f . The measure ν_f is absolutely continuous with respect to Lebesgue measure, but it has zero density at the endpoints of $\widehat{\Sigma}$, that is

$$\nu_f([1 - \epsilon, 1]) \approx \epsilon^{1/\beta} \approx \epsilon^{4.4} \quad \text{as } \epsilon \rightarrow 0. \quad (55)$$

From this analysis we can now conjecture the values of ξ . Following the reasoning as applied in Section IV the conjectural values of ξ are

$$-\frac{1}{\xi} = \dim_H(\nu), \quad \text{for observable (53),} \quad (56)$$

$$-\frac{1}{\xi} = \frac{1}{\beta} + \frac{1}{2} + \tilde{d}_s \quad \text{where } \tilde{d}_s \ll 1 \text{ for observable (54).} \quad (57)$$

The constant \tilde{d}_s comes from the dimension of ν_s which is (numerically) seen to be small due to the strong stable foliation. As in Section V, we replace the Hausdorff dimension with the Lyapunov dimension, which we numerically estimate at $\dim_L \Lambda \approx 2.06$. We take this value to be the estimate of the local dimension of ν . In contrast with the solenoid and Hénon maps, the tail index associated to observable (53) comes from an estimate of the measure of $\nu(L^+(\tilde{u} - \epsilon))$ which we assume scales as the product of the three factors: $\sqrt{\epsilon} \cdot \epsilon^{d_u} \cdot \epsilon^{8d_s}$. Here the factor $\sqrt{\epsilon}$ comes from the measure ν conditioned

on $\Lambda \cap L^+(\tilde{u} - \epsilon)$ in the (central)-flow direction, while the factor ϵ^{d_u} comes from the ν_P -measure conditioned on unstable manifolds that terminate at the cusp. In a generic case we would expect $d_u = 1$. However, since we are near the cusp (namely near the boundary $\partial\widehat{\Sigma}$) we have $d_u = 1/\beta = 4.4$ due to the zero in the density of ν_f , see (55). Finally we have a contributing factor ϵ^{8d_s} that comes from the the strength of the cusp at $P(\partial\Sigma)$, with d_s the local dimension of ν_{γ^s} . We would expect typically that $d_s \approx 0.06$, but it could be much smaller if we are in the vicinity of the cusp.

For the numerical simulations we first consider observable (53), where p_M is a point chosen in the attractor by the same procedure used before, namely selecting the final point of an orbit of length 10^3 time units. The estimates converge to the theoretically expected values of $-1/\dim_L \Lambda \approx -0.5$, see Figure 16 (A). Note that convergence is attained here for block lengths of a few thousands, unlikely what has been observed for the Hénon and Lozi maps. We also obtain convergence to the conjectured value (57) for observable (54), see Figure 16 (B). Also in this case the convergence is much faster than for the Hénon and Lozi maps.

For the Lorenz84 system (52), Lorenz detected a Hénon like structure in a Poincaré section with the plane $y = 0$, see [39, Figures 7 and 8]. If this conjectural structure was correct, then the attractor would coincide with the two-dimensional unstable manifold of a saddle-like periodic orbit of the flow of (52).

Assuming that there is exists an SRB measure ν supported on this attractor, and that there is a local product structure so that ν can be written as $\nu_{\gamma^u} \times \nu_{\gamma^s}$ (as with Lorenz63), then following the reasoning of Section IV the conjectural values of ξ are

$$-\frac{1}{\xi} = \dim_H(\nu), \quad \text{for observable (53).} \quad (58)$$

$$-\frac{1}{\xi} = \frac{\dim_H(\nu_{\gamma^u})}{2} + \dim_H(\nu_{\gamma^s}) \quad \text{for observable (54), with } \dim(\gamma^u) = 2. \quad (59)$$

In this conjecture, it is assumed that the level sets $L^+(\tilde{u} - \epsilon)$ meet the unstable manifolds via generic quadratic tangencies (unlike Lorenz63). The estimates for observable (53) display oscillations around the theoretical value (58), see Figure 17 (A). This behaviour similar to what observed for the Hénon and Lozi maps, see Figs. 11 and 15 (A). The estimates in Figure 17 (B) display oscillations around the value (59): again this is similar to what was observed in the Hénon and Lozi maps, see Figs. 12 and 15 (B).

VII. DISCUSSION AND CONCLUSIONS

This paper has presented an extension of the currently available extreme value theory for dynamical systems to types of observables which are more similar to those found in applications. Namely, the observables considered here are not (necessarily) functions of the distance from a point which is generic with respect to the invariant measure of the chaotic system. Formula (34) and its generalisation (59) were derived under generic assumptions on the geometry of the invariant manifolds underlying the strange attractor. Current research by the Authors aims at formulating explicit conditions under which such formulas hold, both for uniformly and non-uniformly hyperbolic systems. Preliminary findings suggest the following. Suppose we have a system with an attractor $\Lambda \subset \mathbb{R}^d$ that supports a Sinai-Ruelle-Bowen (SRB) measure ν . Moreover suppose that Λ admits a local product structure so that ν can be locally regarded as the product measure $\nu_{\gamma^u} \times \nu_{\gamma^s}$, where ν_{γ^u} (resp. ν_{γ^s}) are the conditional measures on unstable (resp. stable) manifolds. Since ν is SRB, the measures ν_{γ^u} are equivalent to the Riemannian measures on the unstable manifolds, and their local dimension d_u is an integer. The local dimension of ν_{γ^s} is typically non-integer. For sufficiently smooth observables $\phi : \mathbb{R}^d \rightarrow \mathbb{R}$ that have maxima off Λ , we conjecture that the tail index ξ is given by the formula:

$$-\frac{1}{\xi} = \frac{d_u}{2} + d_s. \quad (60)$$

The factor $\frac{d_u}{2}$ comes from assuming that the level sets meet the unstable manifolds in generic (quadratic) tangencies. The factor d_s is the local dimension of ν_{γ^s} . We believe that this dimension d_s is equal to the dimension of the tip set Γ as defined by equation (33). Most of our examples had $\dim_H(\Gamma) < 1$, but in general this could be larger than 1. If this is so, then the projection of Γ onto a line in the direction of $\nabla\phi(\tilde{p})$ would typically have dimension equal to one, and the intersection of Γ with each level set would (typically) be an uncountable set of positive Hausdorff dimension. Thus in addition to studying regularity of unstable holonomies, a careful analysis of the attractor's geometry would be required when estimating the ν -measure of the level regions nearby the extremal point \tilde{p} .

It is of interest to verify the above formula for maps where d_u is larger than one: such is the case for the so-called quasi-periodic Hénon-like attractors [5, 54, 55], which are contained in the closure of the 2D unstable manifold of a saddle-like invariant circle. For flows, this situation corresponds to $d_u = 3$, see e.g. [4]. Also, the Lorenz63 example presented in Section VI shows beyond doubt that the geometry of the attractor can play

a substantial role in determining the limit GEV distribution. In that case the level sets of the observable do not meet the attractor via quadratic tangencies: instead, the level sets meet the attractor at cusps where the measure ν_{γ^u} has a zero. Therefore relation (60) fails to hold and the alternative formula (57) is derived. This situation bears resemblance to the configuration Figure 1 (C) for Thom’s map, which leads to formula (17) for the tail index. Similarly, a modified formula for ξ is expected to hold for the Lozi map under the observable $\phi(x, y) = x$, for which the extremal point \tilde{p} coincides with a cusp-like point in the attractor.

As far as applications are concerned, this paper both points at the further development of useful methodologies and also raises a number of significant questions. We envisage the development of estimation methods for the parameters of the GEV distribution which take into account the information provided by formulas such as (60). Given a concrete system, parameter estimation would be complemented by an analysis of the structure of the attractor to determine appropriate values for d_u and d_s . Specifically, d_u could be estimated by examining Poincaré sections of the attractor and/or finite time Lyapunov exponents. Calculation of Lyapunov exponents would then yield d_s through the relation $\dim_L(\Lambda) = d_u + d_s$, which follows from the local product structure of the invariant measure. Such analysis would also aim to ascertain whether a formula like (60) or appropriate modifications like (57) should be used. This information could be fed into the parameter estimation procedure in an appropriate Bayesian setting.

In the presence of parameter-dependent systems, these formulas provide an explanation for the smooth-like dependence of extreme value statistics with respect to changes in the control parameters. This phenomenon was first observed in [16, 17] and the implications for parameter estimation in non-stationary systems were discussed in [52]. This phenomenon critically depends on the structure of the observables: indeed, for observables like (5) we expect formulas like (60) or (57), which could depend smoothly on control parameters through smooth-like dependence of the attractor dimension on control parameters. On the other hand such smooth-like dependence is rather unlikely to occur for the observables considered so far in the theoretical work, which are of the form (4). Indeed, SRB measures in geophysical systems are usually singular with the Lebesgue measure in phase space, due to dissipation. Therefore, even if the point p_M is generic for the SRB measure for a given value of the control parameters, this situation *is typically not stable* under parameter variation. If p_M is fixed, then one would expect jumps in the value of ξ whenever p_M “drops off” or “drops into” the attractor, see the discussion for Figures 6

and 10.

As far as the questions are concerned, the main one appears to be the extremely slow convergence displayed by the Hénon-like attractors considered here (see e.g. Figures 11, 15–17). Such a slow convergence has been previously observed in more complex atmospheric models, see [51]. Does such a slow convergence take place in state-of-the-art global climate models? This might pose a very serious methodological problem for those studies aiming at quantifying climatic change in extremes, for example changes in the behaviour of hurricanes, wind storms and extreme rainfall.

These problems even raise the following provocative question: how relevant are limit laws for extreme behaviour, if it takes too long for the limit to be attained for any practical purpose? This question may have different answers. One possibility is that novel modelling approaches could be developed to provide more reliable estimates of extreme behaviour, not necessarily restricted to the standard limit laws such as the GEV or the Generalised Pareto distributions [10]. Alternatively, novel parameter estimation procedures might be developed, that incorporate corrections or modifications to account for the phenomena illustrated for Hénon-like attractors, also see Figure 13. The results of this paper seem to suggest that whatever the final answer(s), the methods will have to take into account the geometry and the fractal nature of the strange attractors underlying the dynamics. We believe that these questions and problems will be the subject of significant research efforts in the near future.

Appendix A: Parameter estimation for the GEV distribution

We now describe the procedure which we have used to estimate the parameters μ, σ, ξ of the GEV distribution (2). Consider N_{bmax} values $x_1, \dots, x_{N_{bmax}}$ which we assume to form a random sample from (2). For the systems under consideration, it often turns out that the theoretically expected value of ξ is smaller than -0.5 . In such cases, the standard maximum likelihood approach cannot be used, because the maximum likelihood estimator is not regular [10]. We therefore resort to the method of L-moments [33]. For the GEV

distribution, the L-moments estimation equations are

$$\lambda_1 = \mu - \frac{\sigma}{\xi}(1 - \Gamma(1 - \xi)), \quad (\text{A1})$$

$$\lambda_2 = -\frac{\sigma}{\xi}(1 - 2^\xi)\Gamma(1 - \xi), \quad (\text{A2})$$

$$\frac{\lambda_3}{\lambda_2} = 2\frac{1 - 3^\xi}{1 - 2^\xi} - 3, \quad (\text{A3})$$

see Table 1 in [33]. Given the sample $x_1, \dots, x_{N_{bmax}}$, we use the R package `Lmoments` (<http://cran.r-project.org/>) to estimate the first three L-moments $\lambda_i, i = 1, 2, 3$. Eq. (A3) is then solved for ξ by a Newton method, starting from the initial estimate $\hat{\xi} = 7.859z + 2.9554z^2$, with $z = 2/(3 + \frac{\lambda_3}{\lambda_2}) - \log 2/\log 3$, see Table 2 in [33]. Once an estimate of ξ is obtained, this is plugged into (A2), which is solved for σ . Lastly (A1) is solved for μ .

For the numerical computations, which also include quantifying the estimation uncertainty, we adopt the following procedure. Positive integers N_{bmax} , $N_{blocklen}$ and N_{samp} are fixed: here N_{bmax} is the total number of block maxima to be computed and $N_{blocklen}$ is the length of the data blocks over which each maximum has to be extracted. We first discard a transient of 10^5 iterates with the map under consideration (e.g. the Hénon or the solenoid map). Then a total of $N_{bmax} \cdot N_{blocklen}$ iterates with the map is computed and the N_{bmax} block maxima are extracted. This sample is divided into N_{samp} sub-samples, each containing N_{bmax}/N_{samp} values. We then apply the above L-moment estimation procedure to each sub-sample, thereby obtaining N_{samp} distinct parameter estimates

$$\{(\mu_s, \sigma_s, \xi_s) \mid s = 1, \dots, N_{samp}\}. \quad (\text{A4})$$

The sample means of the estimates (A4):

$$\hat{\mu} = \frac{1}{N_{samp}} \sum_{s=1}^{N_{samp}} \mu_s, \quad \hat{\sigma} = \frac{1}{N_{samp}} \sum_{s=1}^{N_{samp}} \sigma_s, \quad \hat{\xi} = \frac{1}{N_{samp}} \sum_{s=1}^{N_{samp}} \xi_s \quad (\text{A5})$$

are taken as the final GEV parameter estimates and the standard deviations

$$s_\mu^2 = \frac{1}{N_{samp}} \sum_{s=1}^{N_{samp}} (\mu_s - \hat{\mu})^2, \quad s_\sigma^2 = \frac{1}{N_{samp}} \sum_{s=1}^{N_{samp}} (\sigma_s - \hat{\sigma})^2, \quad s_\xi^2 = \frac{1}{N_{samp}} \sum_{s=1}^{N_{samp}} (\xi_s - \hat{\xi})^2 \quad (\text{A6})$$

are taken as estimates of uncertainty for the final values (A5).

Acknowledgments

This research has been carried out within the project ‘‘PREDEX: PREdictability of EXtremes weather events’’, funded by the Complexity-NET: www.complexitynet.eu/. The

Authors gratefully acknowledge support by the UK and Dutch funding agencies involved in the Complexity-NET: the EPSRC and the NWO. P. R. has been partially supported by the MEC grant MTM2009-09723. The Authors are also indebted to their respective Institutes for kind hospitality.

- [1] V. Araujo, M. J. Pacifico, E. R. Pujals, and M. Viana. Singular-hyperbolic attractors are chaotic. *Trans. Amer. Math. Soc.*, 361(5):2431–2485, 2009.
- [2] Jan Beirlant, Yuri Goegebeur, Jozef Teugels, and Johan Segers. *Statistics of Extremes: Theory and Applications*. John Wiley and Sons, Berlin, 2004.
- [3] M. Benedicks and L.-S. Young. Markov extensions and decay of correlations for certain Hénon maps. *Asterisque*, 261:13–56, 2000.
- [4] Henk Broer, Carles Simó, and Renato Vitolo. Bifurcations and strange attractors in the Lorenz-84 climate model with seasonal forcing. *Nonlinearity*, 15(4):1205–1267, 2002.
- [5] Henk Broer, Carles Simó, and Renato Vitolo. Chaos and quasi-periodicity in diffeomorphisms of the solid torus. *Discrete Contin. Dyn. Syst. B*, 14(3):871–905, 2010.
- [6] Henk W. Broer and Floris Takens. *Dynamical systems and chaos*, volume 172 of *Applied Mathematical Sciences*. Springer, New York, 2011.
- [7] H.W. Broer, H.A Dijkstra, C. Simó, A.E. Sterk, and R. Vitolo. The dynamics of a low-order model for the Atlantic Multidecadal Oscillation. *Discrete Contin. Dyn. Syst. B*, 16(1):73–107, 2011.
- [8] Enrique Castillo. *Extreme value theory in engineering*. Statistical Modeling and Decision Science. Academic Press Inc., Boston, MA, 1988.
- [9] J. . Chazottes and P. Collet. Poisson approximation for the number of visits to balls in nonuniformly hyperbolic dynamical systems. *ArXiv e-prints*, July 2010.
- [10] Stuart Coles. *An Introduction to Statistical Modeling of Extreme Values*. Springer Series in Statistics. Springer, New York, 2001.
- [11] P. Collet. Statistics of closest return for some non-uniformly hyperbolic systems. *Ergodic Theory and Dynamical Systems*, 21:401–420, 2001.
- [12] P. Collet and Y. Levy. Ergodic properties of the Lozi mappings. *Comm. Math. Phys.*, 93(4):461–481, 1984.
- [13] Paul Embrechts, Claudia Klüppelberg, and Thomas Mikosch. *Modelling extremal events*, volume 33 of *Applications of Mathematics (New York)*. Springer-Verlag, Berlin, 1997. For insurance and finance.

- [14] Kenneth Falconer. *Fractal geometry*. John Wiley & Sons Inc., Hoboken, NJ, second edition, 2003. Mathematical foundations and applications.
- [15] D. Faranda, V. Lucarini, G. Turchetti, and S. Vaienti. Numerical convergence of the block-maxima approach to the generalized extreme value distribution. Preprint: arXiv:1103.0889v1, 2011.
- [16] Mara Felici, Valerio Lucarini, Antonio Speranza, and Renato Vitolo. Extreme value statistics of the total energy in an intermediate-complexity model of the midlatitude atmospheric jet. part I: Stationary case. *J. Atmos. Sci.*, 64(7):2137–2158, July 2007.
- [17] Mara Felici, Valerio Lucarini, Antonio Speranza, and Renato Vitolo. Extreme value statistics of the total energy in an intermediate-complexity model of the midlatitude atmospheric jet. part II: Trend detection and assessment. *J. Atmos. Sci.*, 64(7):2159–2175, July 2007.
- [18] A. C. M. Freitas. Statistics of the maximum for the tent map. *Chaos Solitons Fractals*, 42(1):604–608, 2009.
- [19] A. C. M. Freitas and J. M. Freitas. On the link between dependence and independence in extreme value theory for dynamical systems. *Statist. Probab. Lett.*, 78(9):1088–1093, 2008.
- [20] A. C. M. Freitas, J. M. Freitas, and M. Todd. Extremal Index, Hitting Time Statistics and periodicity. *ArXiv e-prints*, August 2010.
- [21] A. C. M. Freitas, J. M. Freitas, and M. Todd. Extreme Value Laws in Dynamical Systems for Non-smooth Observations. *ArXiv e-prints*, June 2010.
- [22] A. C. M. Freitas, J. M. Freitas, and M. Todd. Hitting time statistics and extreme value theory. *Probab. Theory Related Fields*, 147(3-4):675–710, 2010.
- [23] Ana Cristina Moreira Freitas and Jorge Milhazes Freitas. Extreme values for benedicks-carleson quadratic maps. *Ergodic Theory Dynam. Systems*, 28(4):1117–1133, 2008.
- [24] J. Galambos. *The asymptotic theory of extreme order statistics*. John Wiley & Sons, New York-Chichester-Brisbane, 1978. Wiley Series in Probability and Mathematical Statistics.
- [25] S. Galatolo and M. J. Pacifico. Lorenz-like flows: exponential decay of correlations for the poincaré map, logarithm law, quantitative recurrence. *Ergodic Theory and Dynamical Systems*, 30:1703–1737, 2009.
- [26] Peter Grassberger and Itamar Procaccia. Measuring the strangeness of strange attractors. *Phys. D*, 9(1-2):189–208, 1983.
- [27] C. Gupta. Extreme value distributions for some classes of non-uniformly partially hyperbolic dynamical systems. Preprint, 2010.
- [28] Chinmaya Gupta, Mark Holland, and Matthew Nicol. Extreme value theory for a class of dynamical systems modeled by young towers. *preprint*, 2009.

- [29] G. Haiman. Extreme values of the tent map process. *Statist. Probab. Lett.*, 65(4):451–456, 2003.
- [30] Boris Hasselblatt and Jörg Schmeling. Dimension product structure of hyperbolic sets. In *Modern dynamical systems and applications*, pages 331–345. Cambridge Univ. Press, Cambridge, 2004.
- [31] M. P. Holland, M. Nicol, and A. Török. Extreme value distributions for non-uniformly hyperbolic dynamical systems. To appear Transactions AMS, 2010.
- [32] Mark Holland and Ian Melbourne. Central limit theorems and invariance principles for Lorenz attractors. *J. Lond. Math. Soc. (2)*, 76(2):345–364, 2007.
- [33] J. R. M. Hosking. L -moments: analysis and estimation of distributions using linear combinations of order statistics. *J. Roy. Statist. Soc. Ser. B*, 52(1):105–124, 1990.
- [34] Yutaka Ishii. Towards a kneading theory for lozi mappings. ii: Monotonicity of the topological entropy and hausdorff dimension of attractors. *Communications in Mathematical Physics*, 190:375–394, 1997. 10.1007/s002200050245.
- [35] James L. Kaplan, John Mallet-Paret, and James A. Yorke. The Lyapunov dimension of a nowhere differentiable attracting torus. *Ergodic Theory Dynam. Systems*, 4(2):261–281, 1984.
- [36] M. R. Leadbetter. Extremes and local dependence in stationary sequences. *Z. Wahrsch. Verw. Gebiete*, 65(2):291–306, 1983.
- [37] M. R. Leadbetter, G. Lindgren, and H. Rootzén. *Extremes and related properties of random sequences and processes*. Springer Series in Statistics. Springer-Verlag, New York, 1983.
- [38] E. N. Lorenz. Deterministic nonperiodic flow. *J. Atmos. Sci.*, 20:130–141, 1963.
- [39] Edward N. Lorenz. Irregularity: a fundamental property of the atmosphere*. *Tellus A*, 36A(2):98–110, 1984.
- [40] Valerio Lucarini, Antonio Speranza, and Renato Vitolo. Parametric smoothness and self-scaling of the statistical properties of a minimal climate model: what beyond the mean field theories? *Phys. D*, 234(2):105–123, 2007.
- [41] C. Masoller, A.C.Sicardi Schifino, and Lilia Romanelli. Regular and chaotic behavior in the new lorenz system. *Physics Letters A*, 167(2):185 – 190, 1992.
- [42] C. Nicolis, V. Balakrishnan, and G. Nicolis. Extreme events in deterministic dynamical systems. *Physical Review Letters*, 97:210602, 2006.
- [43] S. I. Resnick. *Extreme values, regular variation, and point processes*, volume 4 of *Applied Probability. A Series of the Applied Probability Trust*. Springer-Verlag, New York, 1987.
- [44] A. Shil’nikov, G. Nicolis, and C. Nicolis. Bifurcation and predictability analysis of a low-

- order atmospheric circulation model. *Internat. J. Bifur. Chaos Appl. Sci. Engrg.*, 5(6):1701–1711, 1995.
- [45] K. Simon. The Hausdorff dimension of the Smale-Williams solenoid with different contraction coefficients. *Proc. Amer. Math. Soc.*, 125(4):1221–1228, 1997.
- [46] Colin Sparrow. An introduction to the Lorenz equations. *IEEE Trans. Circuits and Systems*, 30(8):533–542, 1983.
- [47] A.E. Sterk, R. Vitolo, H.W. Broer, C. Simó, and H.A. Dijkstra. New nonlinear mechanisms of midlatitude atmospheric low-frequency variability. *Physica D*, 239:702–718, 2010.
- [48] Warwick Tucker. The Lorenz attractor exists. *C. R. Acad. Sci. Paris Sér. I Math.*, 328(12):1197–1202, 1999.
- [49] Lennaert van Veen. Baroclinic flow and the Lorenz-84 model. *Internat. J. Bifur. Chaos Appl. Sci. Engrg.*, 13(8):2117–2139, 2003.
- [50] Lennaert Van Veen, Theo Opsteegh, and Ferdinand Verhulst. Active and passive ocean regimes in a low-order climate model. *Tellus A*, 53(5):616–628, 2001.
- [51] S. Vannitsem. Statistical properties of the temperature maxima in an intermediate order quasi-geostrophic model. *Tellus A*, 59(1):80–95, 2007.
- [52] R. Vitolo, M. P. Holland, and C. A. T. Ferro. Robust extremes in chaotic deterministic systems. *Chaos*, 19:043127, 2009.
- [53] Renato Vitolo, Paolo Ruti, Alessandro dell’Aquila, Mara Felici, Valerio Lucarini, and Antonio Speranza. Accessing extremes of mid-litudinal wave activity: methodology and application. *Tellus A*, 61:35–49, 2009.
- [54] Renato Vitolo, Carles Simó, and Henk Broer. Routes to chaos in the Hopf-saddle-node bifurcation for fixed points of 3D-diffeomorphisms. *Nonlinearity*, 23:1919–1947, 2010.
- [55] Renato Vitolo, Carles Simó, and Henk Broer. Quasi-periodic bifurcations of invariant circles in low-dimensional dissipative dynamical systems. *Regul. Chaotic Dyn.*, 16(1-2):154–184, 2011.
- [56] Renato Vitolo and Antonio Speranza. Vortex statistics in a simple quasi-geostrophic model. *Preprint*, 2011.
- [57] Qiudong Wang and Lai-Sang Young. Toward a theory of rank one attractors. *Ann. of Math. (2)*, 167(2):349–480, 2008.
- [58] Lai-Sang Young. Bowen-Ruelle measures for certain piecewise hyperbolic maps. *Trans. Amer. Math. Soc.*, 287(1):41–48, 1985.
- [59] Lai-Sang Young. What are SRB measures, and which dynamical systems have them? *J. Statist. Phys.*, 108(5-6):733–754, 2002.

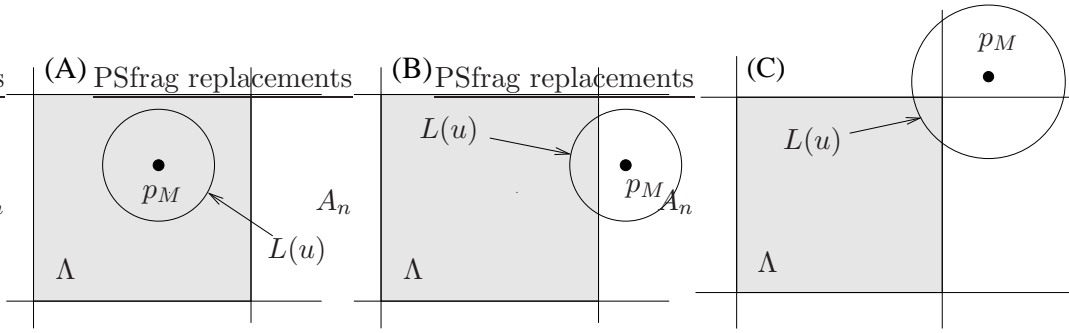


Figure 1: Sketch of the three situations considered in Theorem III.1 for the level sets $L(u)$ (defined in (7)) for observable ϕ_α (13).

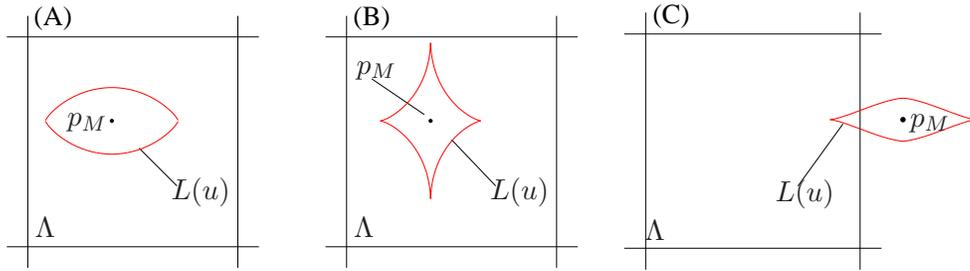


Figure 2: Sketch of a few possible configurations for the level sets $L(u)$ (defined in (7)) for observable ϕ_{ab} (14). (A) $(a, b) = (2, 1.25)$; (B) $(a, b) = (0.5, 0.75)$; (C) $(a, b) = (1.5, 0.7)$.

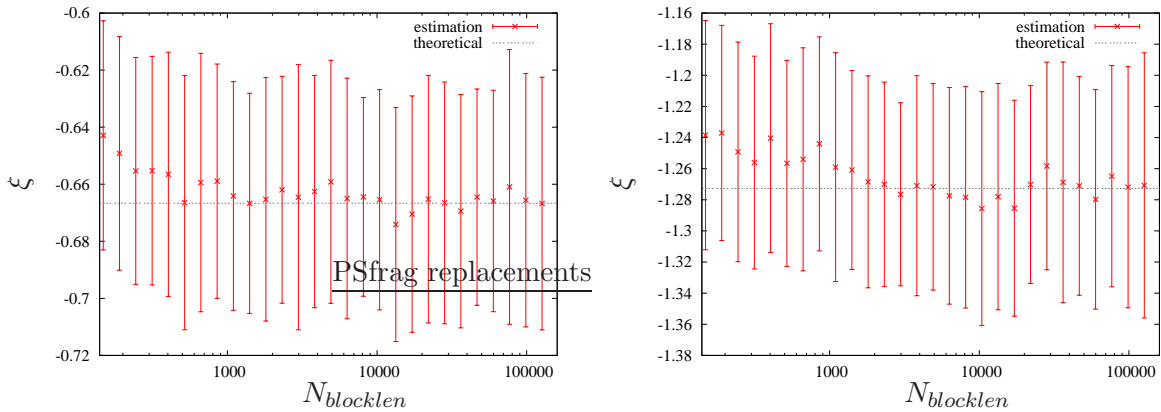


Figure 3: Point estimates (crosses) and estimation uncertainty (vertical bars) of the tail index ξ versus block length $N_{blocklen}$ for Thom's map (12) under the observable (14) with $a = 2$ and $p_M = (0.510001, 0.5090001)$ fixed, where $b/2 = 0.5$ (left) and $b/2 = 1.75$ (right). The horizontal dashed lines represent theoretically expected values according to (18). Crosses and vertical bars are the mean and \pm one standard deviation of a sample of $N_{samp} = 100$ individual estimates along a single orbit. Individual estimates are obtained by the method of L-moments with sequences of $N_{bmax} = 50000$ block maxima over blocks of length $N_{blocklen}$, as described in Appendix A.

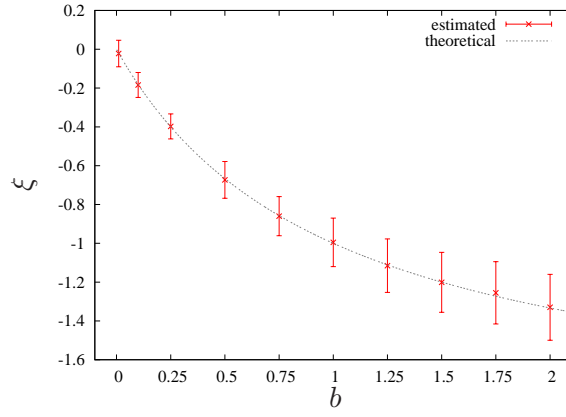


Figure 4: Point estimates (crosses) and estimation uncertainty (vertical bars) of the tail index ξ versus parameter b for Thom's map (12) under the observable (14) with $a = 2$ and $p_M = (0.510001, 0.5090001)$ fixed and varying $b/2 = 0.01, 0.1, 0.25, 0.5, 0.75, 1, 1.25, 1.5, 1.75, 2$. The dashed line represents theoretically expected values according to (18). Point and interval estimates are obtained by the method of L-moments as for Figure 4, with $N_{bmax} = 10000$, $N_{blocklen} = 10000$ and $N_{samp} = 100$, see Appendix A.

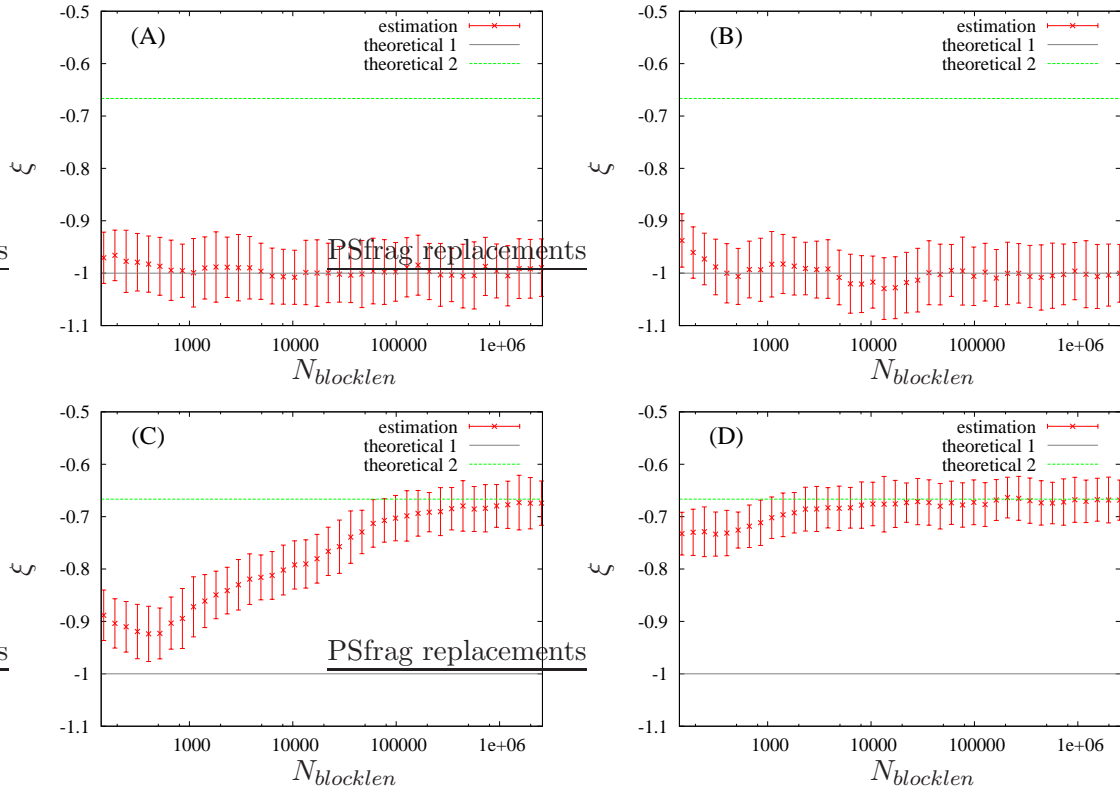


Figure 5: Point estimates (crosses) and estimation uncertainty (vertical bars) of the tail index ξ versus block length $N_{blocklen}$ for Thom's map (12) under the observable (13) with $\alpha = 1$ and $p_M = (x_M, y_M)$ with $y_M = 0.510001$ fixed and (A) $x_M = 0.9$, (B) $x_M = 1.0$, (C) $x_M = 1.01$, (D) $x_M = 1.1$. Horizontal lines labelled by 1, 2 represent theoretical values according to (15) and (16), respectively. Estimates are obtained by the method of L-moments as for Figure 4, with $N_{bmax} = 50000$ and $N_{samp} = 100$, see Appendix A.

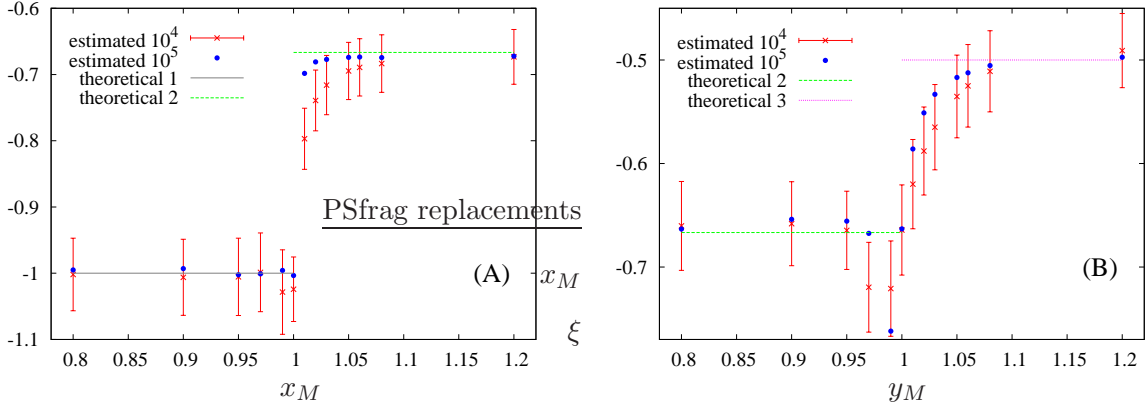


Figure 6: Point estimates (crosses) and estimation uncertainty (vertical bars) of the tail index ξ for Thom's map (12) under the observable (13) with $\alpha = 2$ and (A) $y_M = 0.5090001$ and x_M varying, and (B) $x_M = 1.2$ and y_M varying. Horizontal lines labelled by 1, 2, 3 represent theoretical values according to (15), (16) and (17), respectively. The method of L-moments was used as described in Appendix A with $N_{bmax} = 10000$ and $N_{samp} = 100$ fixed, with $N_{blocklen} = 10^4$ (red) and $N_{blocklen} = 10^5$ (blue).

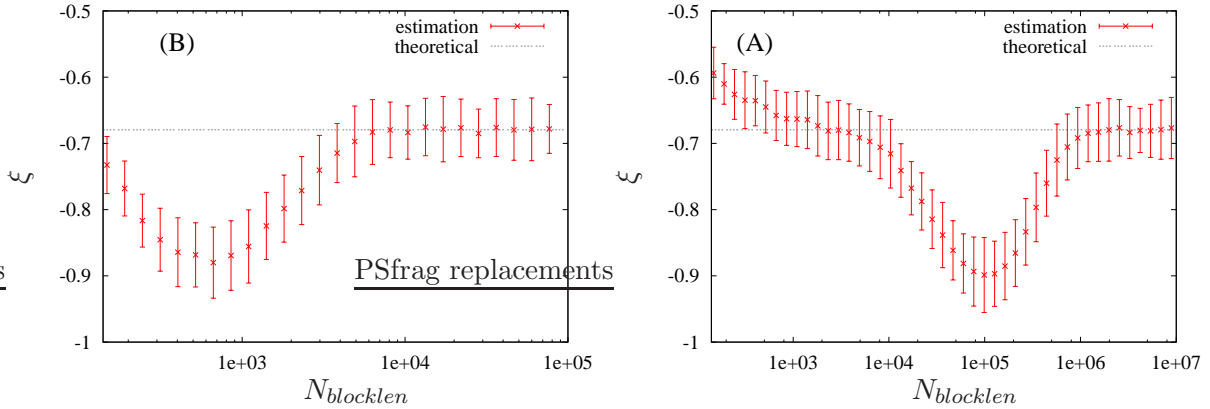


Figure 7: Point estimates (crosses) and estimation uncertainty (vertical bars) of the tail index ξ versus block length $N_{blocklen}$ for the Solenoid map (27) under the observable (38) (left) and (39) (right) with $\theta = 0.5$. The horizontal dashed lines represent theoretically expected values according to (34) Estimates are obtained by the method of L-moments as for Figure 4, with $N_{bmax} = 10000$ and $N_{samp} = 100$, see Appendix A.

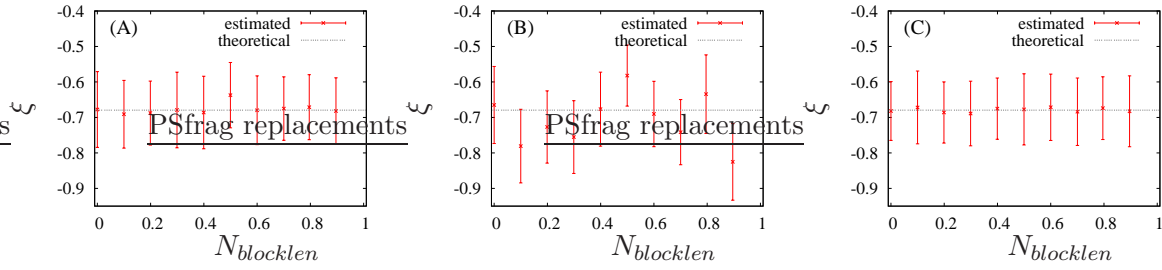


Figure 8: Point estimates (crosses) and estimation uncertainty (vertical bars) of the tail index ξ versus parameter θ for the solenoid map (27) under the observable (38) (A) and (39) (B,C) with $x_0 = y_0 = z_0 = 3$, where $\theta = \frac{i}{10}$ for $i = 0, \dots, 9$. The dashed line represents theoretically expected values according to (34). Estimates are obtained by the method of L-moments as for Figure 4, with $N_{bmax} = 10000$ and $N_{samp} = 100$, see Appendix A, where $N_{blocklen} = 10000$ (A,C) and $N_{blocklen} = 10^6$ (B).

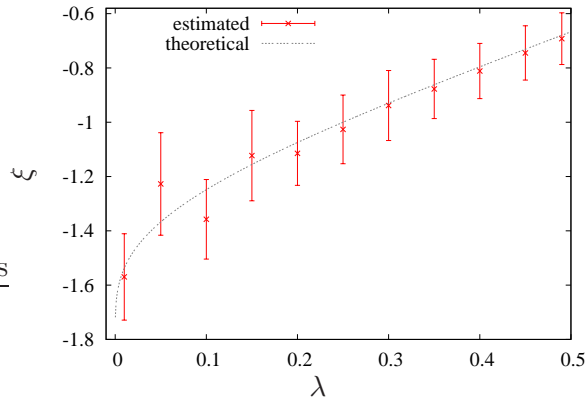


Figure 9: Point estimates (crosses) and estimation uncertainty (vertical bars) of the tail index ξ versus parameter λ for the solenoid map (27) under the observable (38) with $\theta = x_0 = y_0 = 0$. The dashed line represents theoretically expected values according to (34). Estimates are obtained by the method of L-moments as for Figure 4, with $N_{bmax} = 50000$, $N_{samp} = 100$ and $N_{blocklen} = 10000$, see Appendix A.

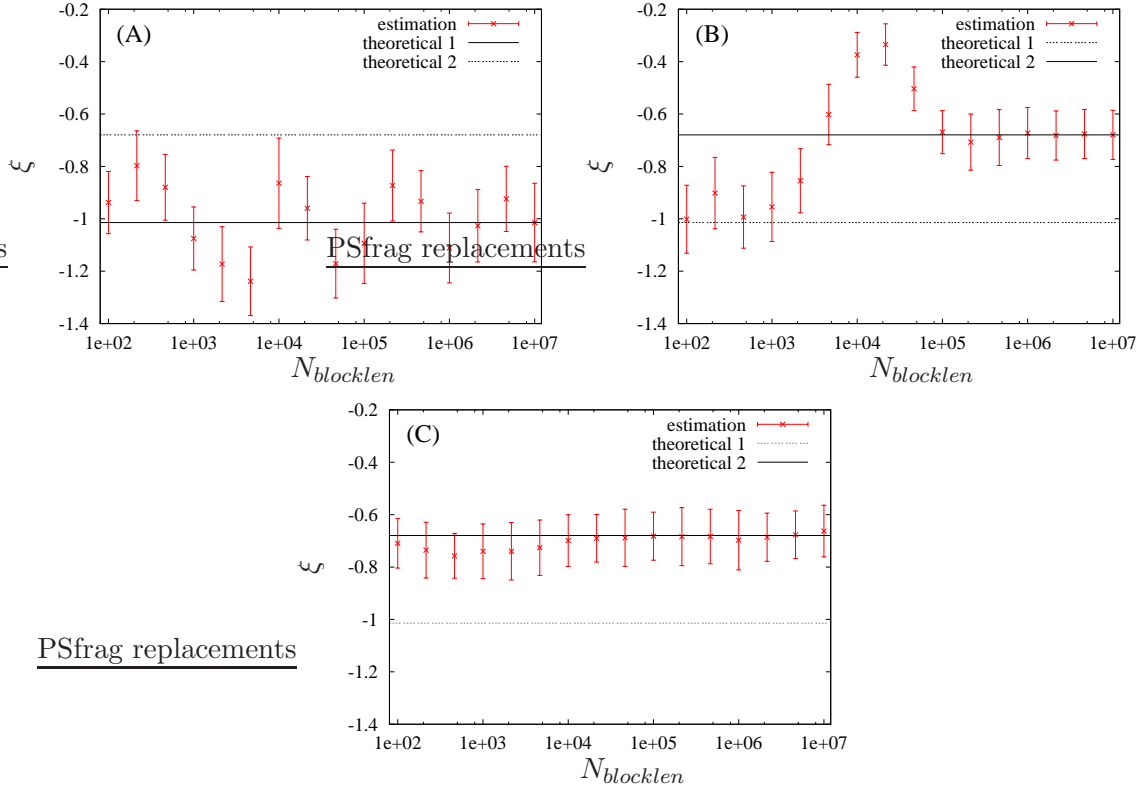


Figure 10: Point estimates (crosses) and estimation uncertainty (vertical bars) of the tail index ξ versus block length $N_{blocklen}$ for the solenoid map (27) under the observable (29) with $\alpha = 0.3$. (A) p_M is chosen as a point $p_M^0 \in \Lambda$ as described in the text. (B) $p_M = p_M^t = (1+t)p_M^0$ with $t = 0.1$. (C) $p_M = p_M^t$ with $t = 1$. The dashed lines represent theoretically expected values according to (15) Estimates are obtained by the method of L-moments as for Figure 4, with $N_{bmax} = 10000$ and $N_{samp} = 100$, see Appendix A.

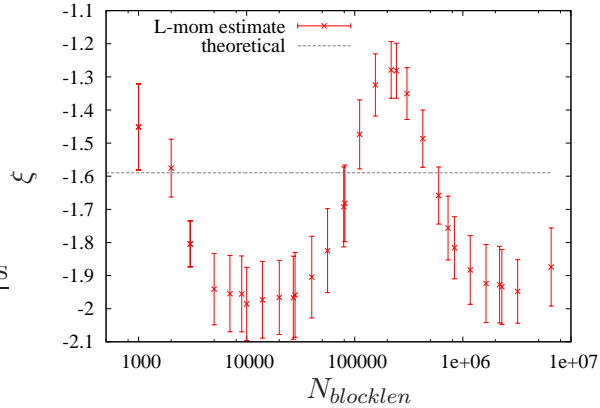


Figure 11: Point estimates (crosses) and estimation uncertainty (vertical bars) of the tail index ξ versus block length $N_{blocklen}$ for the Hénon map (40) under the observable (42) with $\alpha = 2$. The horizontal dashed line represents theoretically expected values according to (44), with the Lyapunov dimension replacing the Hausdorff dimension, see text. Estimates are obtained by the method of L-moments as for Figure 4, with $N_{bmax} = 50000$ and $N_{samp} = 100$, see Appendix A.

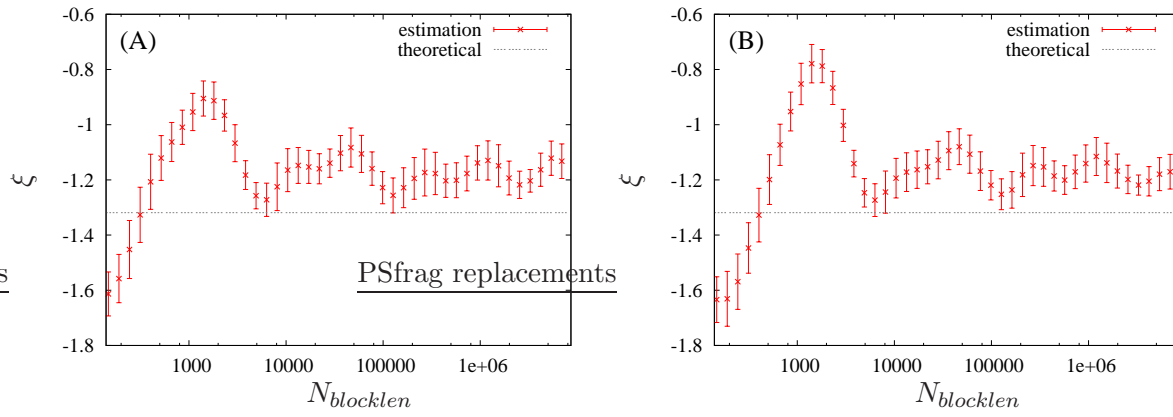


Figure 12: Point estimates (crosses) and estimation uncertainty (vertical bars) of the tail index ξ versus block length $N_{blocklen}$ for the Hénon map (40) under the observable (43) with $\theta = 0$ (left) and $\theta = 0.5$ (right). The horizontal dashed lines represent theoretically expected values according to (45). Estimates are obtained by the method of L-moments as for Figure 4, with $N_{bmax} = 10000$, and $N_{samp} = 100$, see Appendix A.

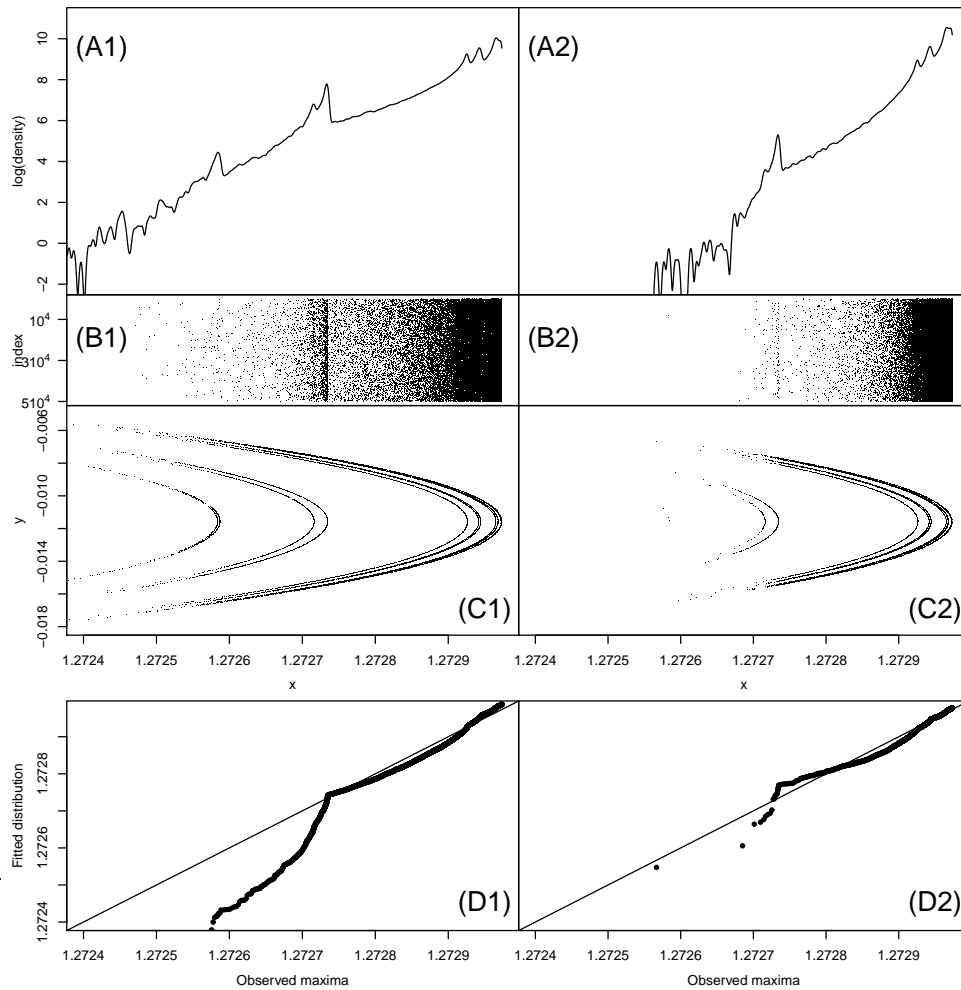


Figure 13: Diagnostics of the GEV distribution fit for the Hénon map (40) under observable (43) with $\theta = 0$, with $N_{bmax} = 5 \cdot 10^5$ block maxima computed over blocks of length $N_{blocklen} = 5 \cdot 10^4$ (left column, A1-D1) and $N_{blocklen} = 1.2 \cdot 10^5$ (right column A2-D2). (A1,2) Non-parametric log-densities of the block maxima, obtained by Gaussian kernel smoothing with bandwidth 0.000002. (B1,2) Time series of the $5 \cdot 10^4$ block maxima (with the block sequential index on the vertical axis). (C1,2) Points on the Hénon attractor corresponding to the block maxima used in (A1) and (A2), respectively. (D1,2) Quantile-quantile plot of the empirical distribution of the block maxima (horizontally) versus the fitted GEV distribution.

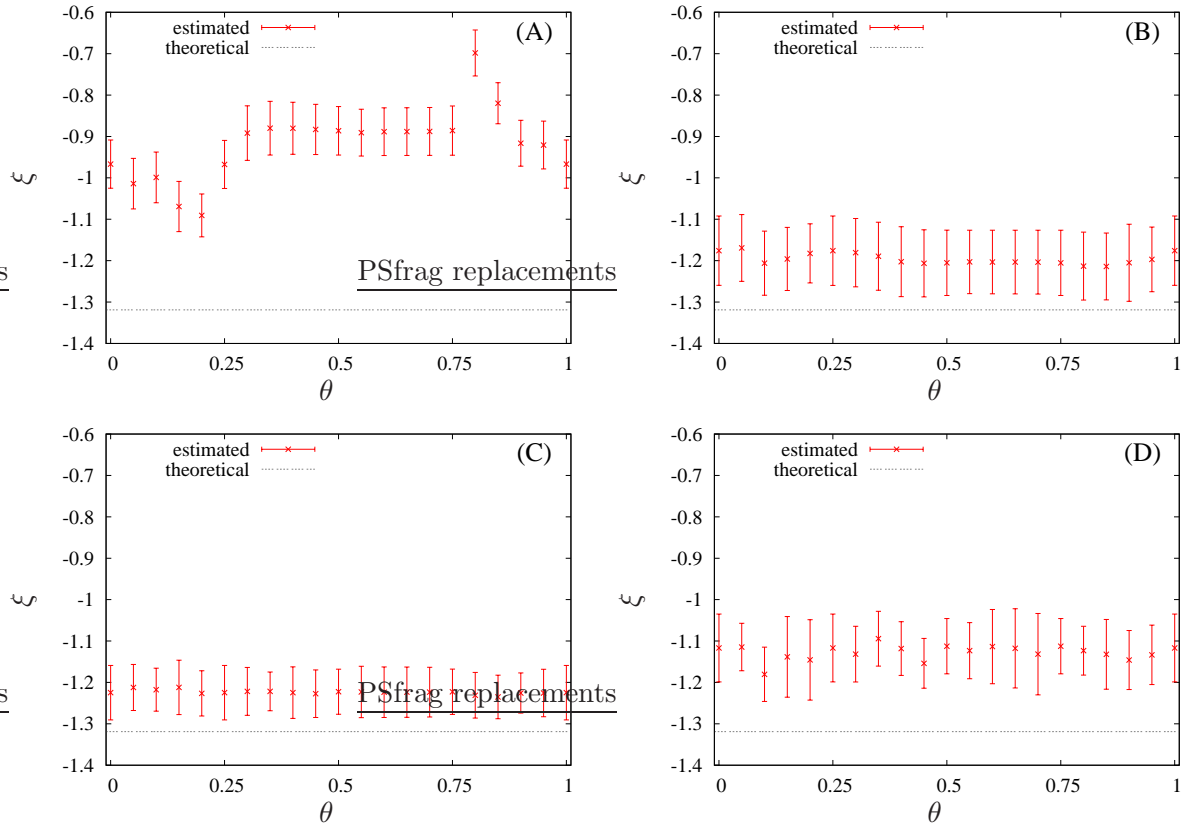


Figure 14: Point estimates (crosses) and estimation uncertainty (vertical bars) of the tail index ξ versus θ for the Hénon map (40) under the observable (43) for block lengths of (A) $N_{blocklen} = 10^3$, (B) $N_{blocklen} = 10^4$, (C) $N_{blocklen} = 10^5$, (D) $N_{blocklen} = 10^6$. The horizontal dashed lines represent theoretically expected values according to (45). Estimates are obtained by the method of L-moments as for Figure 4, with $N_{bmax} = 10^5$, and $N_{samp} = 100$, see Appendix A.

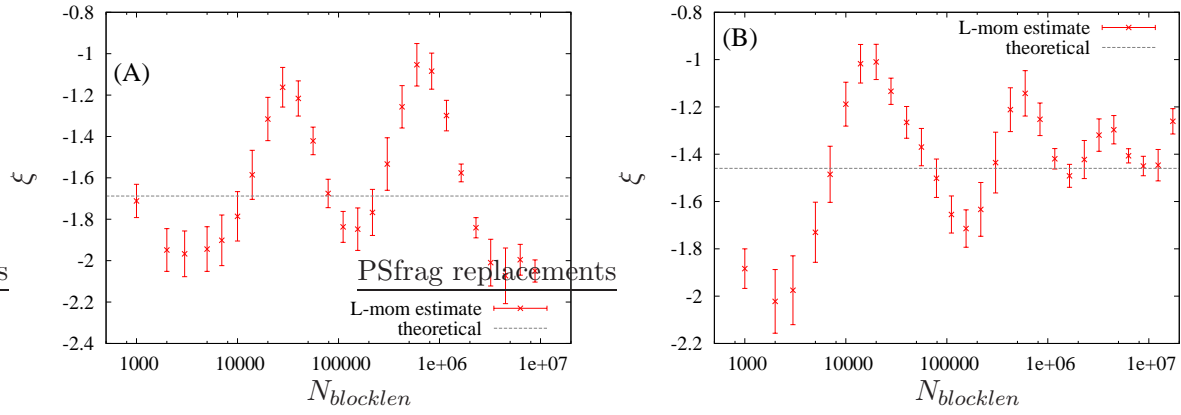


Figure 15: Point estimates (crosses) and estimation uncertainty (vertical bars) of the tail index ξ versus block length $N_{blocklen}$ for the Lozi map (40) under the observable (42) with $\alpha = 2$ and (A) for a point p_M belonging to the attractor; (B) for $p_M = (0.2, 0.01)$. The horizontal dashed line represents theoretically expected values according to (44), with the Lyapunov dimension replacing the Hausdorff dimension, see text. Estimates are obtained by the method of L-moments as for Figure 4, with $N_{bmax} = 50000$ and $N_{samp} = 100$, see Appendix A.

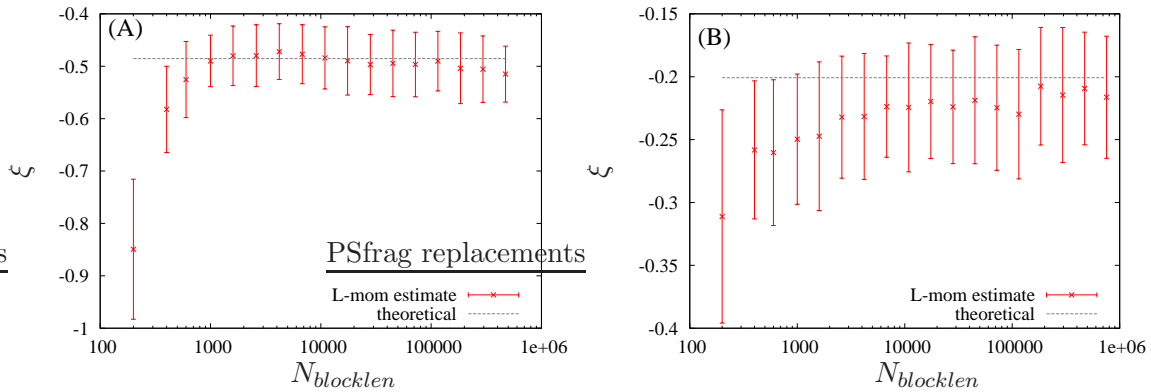


Figure 16: Point estimates (crosses) and estimation uncertainty (vertical bars) of the tail index ξ versus block length $N_{blocklen}$ for the Lorenz63 flow (51) (A) under the observable (53) where p_M is chosen as the final point of an orbit of length 10^3 time units starting from an arbitrary point, and (B) under observable (54). Horizontal lines represent theoretical values. Estimates are obtained by the method of L-moments as for Figure 4, with $N_{bmax} = 20000$ and $N_{samp} = 100$, see Appendix A.

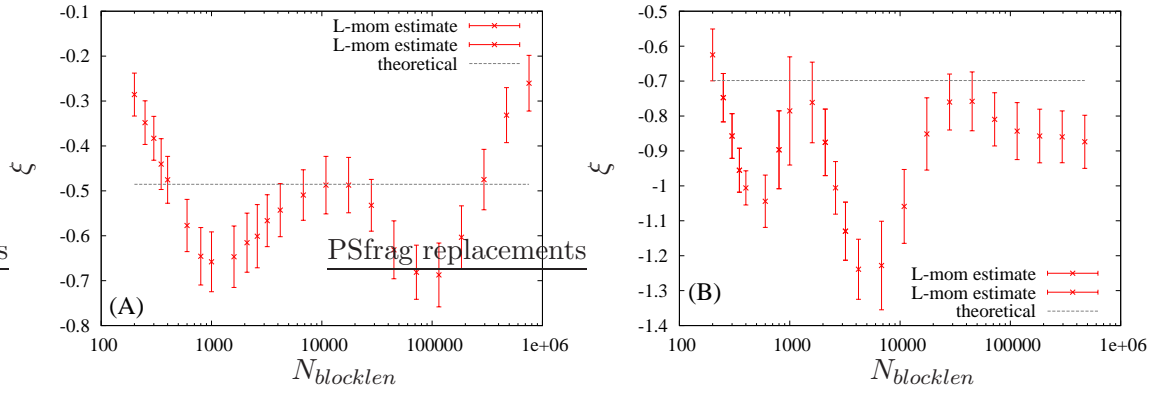


Figure 17: Point estimates (crosses) and estimation uncertainty (vertical bars) of the tail index ξ versus block length $N_{blocklen}$ for the Lorenz63 flow (51) (A) under the observable (53) where p_M is chosen as the final point of an orbit of length 10^3 time units starting from an arbitrary point, and (B) under observable (54). Horizontal lines represent theoretical values according to (58) (A) and (59) (B). Estimates are obtained by the method of L-moments as for Figure 4, with $N_{bmax} = 20000$ and $N_{samp} = 100$, see Appendix A.